České vysoké učení technické v Praze
Fakulta jaderná a fyzikálně inženýrská

Katedra fyziky
Obor: Experimentální jaderná a částicová fyzika

Produkce mezonu Upsilon na experimentu STAR

Upsilon Production at the STAR Experiment

BAKALÁŘSKÁ PRÁCE

Vypracoval: Robert Líčeník
Vedoucí práce: Ing. Olga Rusňáková, Ph.D.
Rok: 2017

Czech Technical University in Prague
Faculty of Nuclear Sciences and Physical Engineering

Department of Physics
Specialization : Experimental Nuclear and Particle Physics

Produkce mezonu Upsilon na experimentu STAR

Upsilon Production at the STAR Experiment

BACHELOR THESIS

Author: Robert Líčeník
Supervisor: Ing. Olga Rusňáková, Ph.D.
Year: 2017

Před svázáním místo téhle stránky $\boxed{\text{vložíte zadání práce}}$ s podpisem děkana (bude to jediný oboustranný list ve Vaší práci) !!!!

Prohlášení

Prohlašuji, že jsem svou bakalářskou práci vypracoval samostatně a použil jsem pouze podklady (literaturu, projekty, SW atd.) uvedené v přiloženém seznamu.

Nemám závažný důvod proti použití tohoto školního díla ve smyslu § 60 Zákona č. 121/2000 Sb., o právech souvisejících s právem autorským a o změně některých zákonů (autorský zákon).

V Praze dne ....

....
Robert Líčeník

Acknowledgments

I would like to thank the supervisor of my thesis, Dr. Olga Rusňáková, for guiding me and helping me throughout the entire process. I would also like to thank Jan Rusňák for his time and advice which made the completion of this thesis possible.

Robert Líčeník

Název práce:
Produkce mezonu Upsilon na experimentu STAR

Autor: Robert Líčeník

Obor: Experimentální jaderná a částicová fyzika

Druh práce: Bakalářská práce

Vedoucí práce: Ing. Olga Rusňáková, Ph.D.
Katedra fyziky,
Fakulta jaderná a fyzikálně inženýrská,
České vysoké učení technické v Praze

Abstrakt: Mezon Υ *představuje významnou sondu v kvark-gluonovém plazmatu, které vzniká při vysokoenergetických jádro-jaderných srážkách, jelikož je jeho produkce potlačena z důvodu barevného stínění. Výsledky jeho produkce poté pomáhají s vytvářením fázového diagramu silně interagující hmoty. Boužel se signál tohoto mezonu ve srážkách Au-Au při* $\sqrt{s_{NN}} = 200$ *GeV, detekovaných na experimentu STAR, zatím nepodařilo úspěšně zrekonstruovat.*

Klíčová slova: kvarkonia, Υ mezon, srážky těžkých iontů, kvark-gluonové plazma, experiment STAR

Title:
Upsilon Production at the STAR Experiment

Author: Robert Líčeník

Specialization: Experimental Nuclear and Particle Physics

Sort of Thesis: Bachelor Thesis

Supervisor: Ing. Olga Rusňáková, Ph.D.
Department of Physics,
Faculty of Nuclear Sciences and Physical Engineering,
Czech Technical University in Prague

Abstract: The Υ meson is a significant probe in the quark-gluon plasma, which is created during high-energy nucleus-nucleus collisions, since its production is suppressed as a consequence of the color screening. The results of the meson production help with creating the phase diagram of the strongly-interacting matter. Unfortunately, the meson's signal in the Au-Au collisions at $\sqrt{s_{NN}} = 200$ GeV detected by the STAR experiment has not been successfully reconstructed so far.

Key words: quarkonia, Υ meson, heavy ion collisions, quark-gluon plasma, STAR experiment

Contents

List of Figures

Introduction

The model which current science uses the most to describe the Universe is the Standard Model. According to this model, all matter in the Universe is composed of quarks and leptons and is governed by the three fundamental interactions - electromagnetic, strong and weak. The electromagnetic force has limitless range (because its gauge boson, photon, is massless), following the inverse-square law. However, only electrically charged particles are affected by it. The strong force is the strongest interaction, but has a limited range, about the size of an atomic nucleus, and acts on particles carrying a color charge (quarks and gluons) only. The weak interaction acts on even shorter distances (shorter than the proton radius), is relatively weak compared to the others and has the ability to change quark flavor. The fourth fundamental interaction - gravity, which acts on all massive particles - is not included in the Standard Model. Each interaction is characterized by its coupling constant, which carries information about the interaction's relative strength and the probability that certain particle will interact via that interaction (assuming the interaction is possible). The approximate ratios of these coupling constants are: $\alpha_s : \alpha : \alpha_w : \alpha_g =$ 1:$\frac{1}{137}$:10^{-7}:10^{-39}. The quarks and leptons together with interaction bosons and the Higgs boson (responsible for other particles' mass) are called elementary particles (Fig. 1).

The Higgs boson, experimentally confirmed in 2013 by the ATLAS and the CMS collaborations [2], was the last particle predicted by the Standard Model. There are six quark flavors (up, down, charm, strange, top and bottom) and also six different leptons (the electron, the muon, the tau and corresponding neutrinos). Both quarks and leptons do interact weakly, by emission/absorption of $W^{\pm}$ or Z^0 bosons. In the Standard Model frame, the neutrinos are thought to be massless, even though recent observations suggest otherwise (NP 2015, [3], [4]), and carry no charge. The other leptons do carry a charge of -1 e (the elementary charge) and do have non-zero mass. All leptons are colorless. All quarks are charged (+2/3 of the elementary charge or -1/3 of the elementary charge), implying that they interact via the electromagnetic force by exchanging photons. Moreover, the quarks are massive and also carry a color charge (red, green or blue) and thus interact strongly by exchanging gluons. Even though the quarks can only exist confined in hadrons (mesons and baryons), they can be observed as free in the quark-gluon plasma (QGP, section 1.3)

The main objective of heavy ion collisions (sections 1.1, 1.2) and this thesis is to study fundamental properties of elementary particles and the interactions among them.

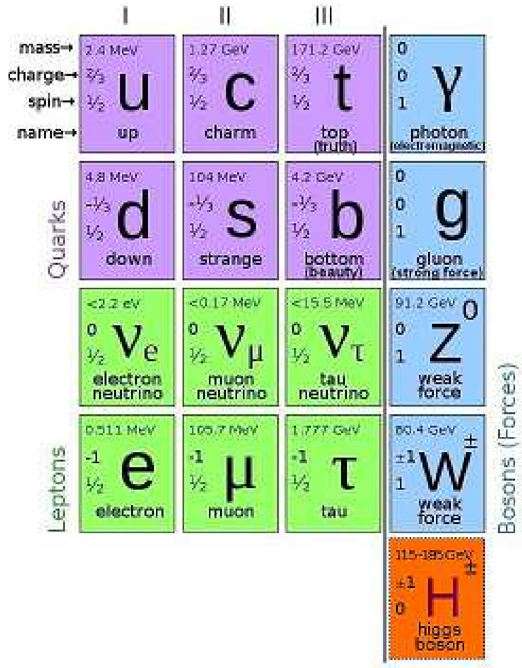

Figure 1: Table showing all predicted elementary particles. All of them have been experimentally confirmed. A corresponding antiparticle exists for each one. Source: [1].

Chapter 1

Introduction to Heavy Ion Collisions

Heavy ion collisions are collisions of two heavy atomic nuclei accelerated to velocities close to the speed of light in vacuum ($c = 299,792,458$ ms^{-1}). Different nuclei are used, notably Cu, Au, U (RHIC) and Pb (LHC). For a certain nucleus to be used, one or more of the following qualities is required: large number of nucleons, large nucleon density and/or very spherical shape. Every collision is characterized by its centrality (sec. 1.1) and this then affects the evolution of the system (sec. 1.2), whether the QGP (sec. 1.3) is formed and how significant the difference between an A-A and a p-p collision is (sec.1.5). The ultimate objective of the heavy-ion collision studies is to obtain a QCD matter phase diagram (sec. 1.4).

1.1 Collision Centrality

When two nuclei collide, they rarely collide "head-on". Instead, the area in which the nuclei overlap is basically random. The nucleons in the overlapping region are called participants, the others are called spectators and are not important for the collision. This overlap is characterized by a parameter b called the impact parameter. The impact parameter is defined as the distance between the centers of both nuclei (Fig. 1.1).

Depending on b, the collision is classified as central ($b \simeq 0$), peripheral ($2R_A > b > 0$), where R_A is the radius of the nucleus, and ultra-peripheral ($b > 2R_A$). Since it is impossible to measure b directly, one common way to determine b is to introduce multiplicity. Multiplicity is the measurement of particles participating in the collision. This measurement produces an event count dependence on the total deposited energy of the event (as seen in Fig. 1.2) or on the number of participants.

One of the theoretical models describing the collision centrality is the Glauber model [7]. However, its details are beyond the scope of this thesis.

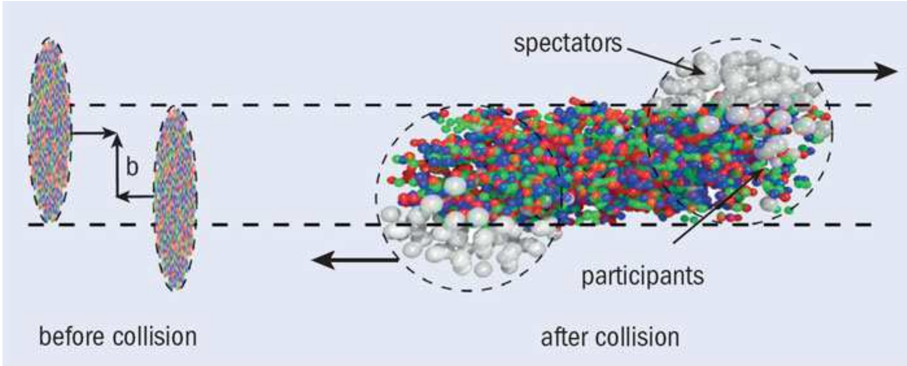

Figure 1.1: Illustration of a nucleus-nucleus collision. Shown are participants, spectators and impact parameter b of the collision. Source: [5].

1.2 Collision Evolution

When two ultrarelativistic heavy atomic nuclei collide, it can be assumed that the participants collide "one-on-one". The nucleons scatter and a hot dense system - called fireball - is formed. At a sufficient energy density, new particles are being created from the vacuum. In this period - the hard scattering - the system is not in thermal equilibrium. Shortly afterwards, the energy density and therefore the temperature is high enough for the deconfinement to set in, resulting in a new state of matter called the QGP. This system is then in thermal equilibrium and it is following hydrodynamic laws for a superfluid that cools down and expands in time and space. When the temperature decreases below the confinement temperature T_c, a new process - the hadronization - sets in. In this process, the matter further cools down and expands. The quarks cannot be free anymore and are confined in baryons and mesons together with gluons. The created hadrons interact among themselves as the temperature decreases further, until the interactions stop. The point in space-time where the hadrons do not interact anymore is called freeze-out. The final products (leptons, pions, kaons, protons and photons) are then captured in the detector. This process is illustrated in Fig. 1.3.

The space-time evolution of a high-energy heavy-ion collision is illustrated in Fig. 1.4

1.3 Quark-gluon Plasma

Quark-gluon plasma (QGP) is a state of matter, where quarks and gluons are not confined in hadrons anymore, but are free instead. The early Universe (between the end of the inflation period and hadronization, $t \sim 10^{-6}$ s) is thought to be precisely in this state of hot, dense matter. QGP is not observable anywhere in the present Universe, except for brief time periods after nucleus-nucleus (A-A) collisions in particle accelerators. The existence of the QGP was experimentally confirmed in 2004 at RHIC ([10]). Many physical properties of the QGP have not been determined

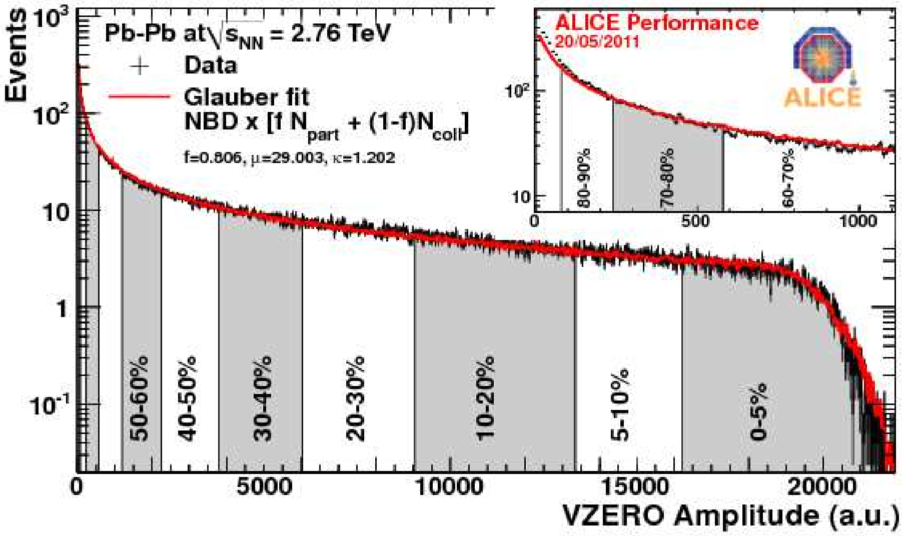

Figure 1.2: ALICE 2.76 TeV measurements of multiplicity in Pb-Pb collisions. Particle count is plotted against the ALICE V0 detector signal strength, proportional to collision energy. Data are fitted by a Glauber model calculation. Source: [6].

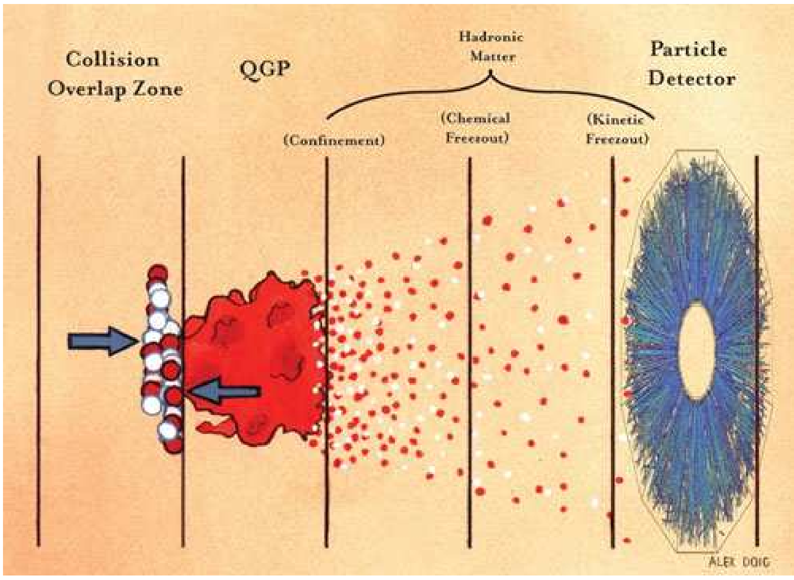

Figure 1.3: An image showing the time evolution of the stages in a heavy ion collision. The hadronization period is further divided into two smaller time intervals, before and after chemical freeze-out. Source: [8].

yet. However, it is expected to behave at least partially in ways similar to ideal fluids.

The theoretical model describing strong interaction and therefore the physical aspect of QGP formation is the quantum chromodynamics (QCD). It concerns itself with interactions between quarks and gluons as they are the only particles that have a quantum number called color (charge). Quarks carry one color (red, green, blue), while gluons carry a combination of one color and one anticolor and bind quarks to-

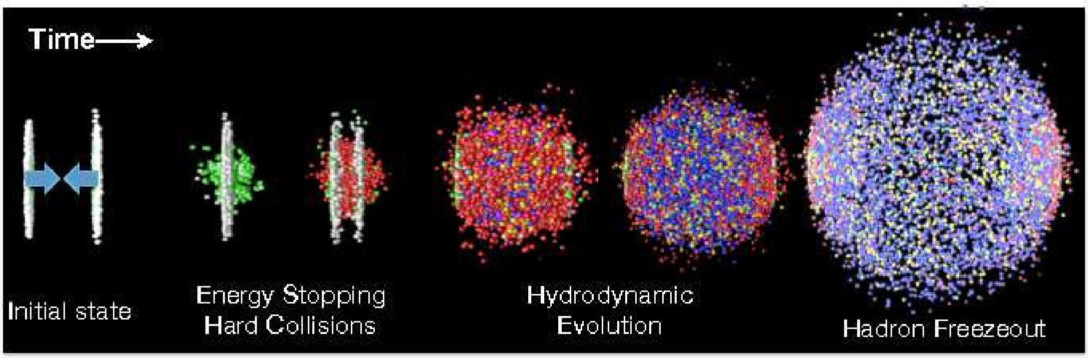

Figure 1.4: Time-space high-energy heavy-ion collision evolution illustration. QGP is present in the third stage. Source: [9].

gether to form hadrons. As the law of conservation of color charge states, all hadrons must be color-neutral/colorless. This means that baryons have to be composed of 3 quarks, one of each color (antibaryons are composed of 3 antiquarks, one of each anticolor), while mesons are composed of a colored quark and an antiquark of the corresponding anticolor. The characteristic time of the strong interaction is $\tau \sim 10^{-23}$ s. The strong force is parametrized by a strong interaction coupling constant

$$\alpha_s(Q) = \frac{12\pi}{(33 - 2N_f)\ln\frac{Q^2}{\lambda_{QCD}}}, \tag{1.1}$$

where N_f is the number of quark flavors, Q^2 is the four momentum transfer and $\lambda_{QCD} \simeq 0.2$ GeV is the typical QCD scale, obtained experimentally, [11]. The main characteristic of the strong interaction coupling constant is that it is not constant, but rather dependent on the energy of the system, its temperature and distance over which the two partons (q, g) interact. The dependence on momentum (therefore on energy and temperature as well) can be seen in Fig. 1.5.

This property has an interesting implication. Provided the energy is high enough, the quarks and gluons are not confined in hadrons anymore, but rather allowed to exist in a deconfined state. The parameter characterizing this sufficient energy is the critical temperature ($T_c = 140 - 200$ MeV, depending on calculation, [13, 14, 15]). When reached, the quarks and gluons can be free and the medium is called QGP. The temperature needed for deconfinement is not universal, but rather dependent on the actual particle. For example, for a $\Upsilon(3S)$ to dissolve, $T > T_c$ is sufficient, for $\Upsilon(2S)$ or J/ψ, $T > 1.2\ T_c$ is required and for $\Upsilon(1S)$, $T > 2\ T_c$ is needed. This lead to the idea of quarkonium thermometer, which can be seen in Fig. 1.6. This phenomenon would then lead to observations of quarkonia production suppression in heavy ion collisions. First to propose this idea were Matsui and Satz in 1986, [17].

This observed phenomenon is consistent with another expected behavior - the asymptotic freedom. The strong interaction coupling constant depends on the distance between the two particles and this dependence is directly proportional meaning that

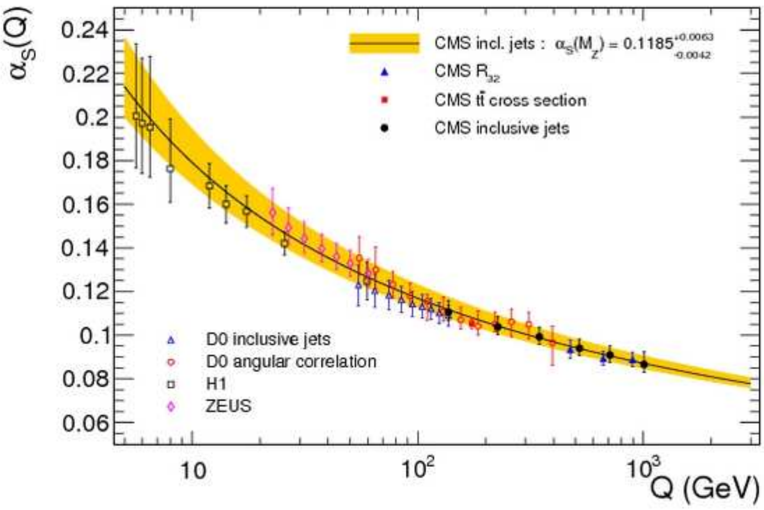

Figure 1.5: The strong interaction coupling constant α_s dependence on momentum. CMS experimental data compared to QCD calculation. $\alpha_s(M_Z)$ is the value at Z^0 mass, world average. Source: [12].

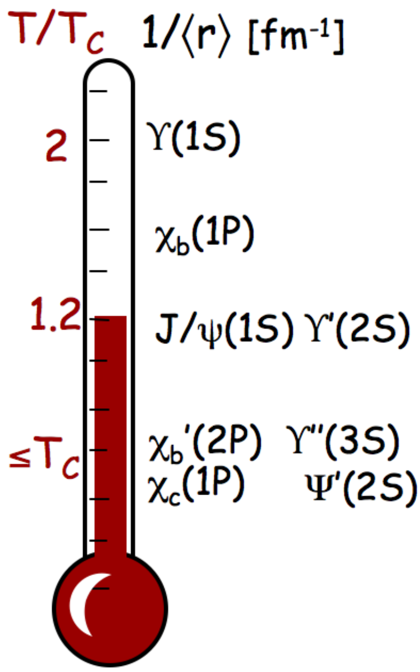

Figure 1.6: The quarkonium thermometer illustration, showing approximate temperatures required for different quarkonia to dissolve. Source: [16].

α_s increases, when the two particles move apart, resulting in a situation where it is more energetically favorable to create a new quark-antiquark pair from vacuum than to continue the separation. On the other hand, at short distances ($r < r_c \sim 0.5$ fm), the quarks are no longer bound.

Because of the QGP's extremely short lifetime, it is impossible to observe and study it directly. One way to study the properties and obtain desired thermodynamic variables of the QGP is using probes. There are three types of QGP probes: soft (such as flow and fluctuations, [18]), electromagnetic (photons and dileptons, [19]) and hard (jet quenching, quarkonium suppression). The following subsections will expand on several of the probes mentioned above.

1.3.1 Elliptic Flow

Because the A-A collisions are rarely head-on (see sec. 1.1), the participant distribution is not uniform, but rather anisotropic. This means that a pressure gradient is present, resulting in a flow of the hot matter. This initial anisotropy and subsequent evolution is illustrated in Fig. 1.7. The elliptic flow is then measured as an anisotropic momentum distribution of particles.

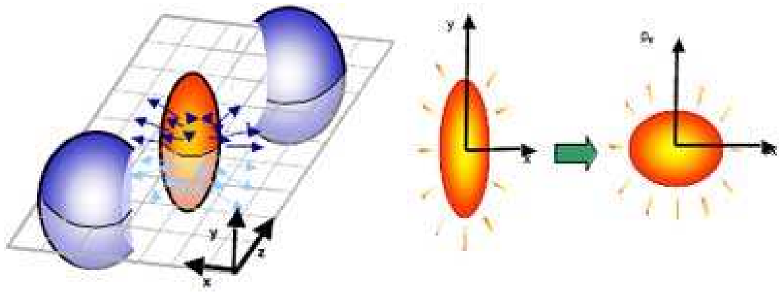

Figure 1.7: Left: The active collision zone between two nuclei. Right: The initial anisotropy of the collision zone and its evolution into the final-state elliptic flow. Source: [20].

Flow is characterized by flow coefficients v_n. These coefficients are present in the Fourier series expansion of the particle distribution function (see [21]). An elliptic flow coefficient v_2 is expected to be negligible in events where no hot dense ideal-fluid-like matter is present. The RHIC results (Fig. 1.8) of elliptic flow measurements indicate strong elliptic flow at higher p_T and therefore provide another evidence of QGP formation and existence. For further details on elliptic flow or flow in general see [21], [22].

1.3.2 Jet Quenching

A jet is a narrow collimated bunch of particles with large transverse momentum. It is a final product of a parton hard scattering as a result of fragmentation and hadronization processes. As the parton scatters it radiates a few gluons and the system hadronizes, creating a collimated spray of hadrons - jet. The observation of jets is then used as an indicator of high energy events. Jets are usually observed in binary events called dijets. When a dijet is formed on the edge of the fireball - system of hot dense nuclear matter created right after the two nuclei collide - one

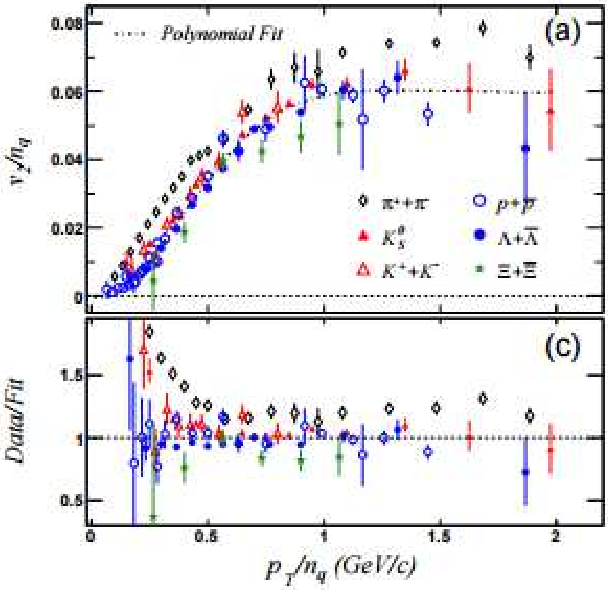

Figure 1.8: RHIC v_2 flow dependence on p_T measurement at $\sqrt{s_{NN}}$ = 62.4 GeV Au-Au collisions. Data are scaled by quark number and fitted by a polynomial. The rise in flow at higher p_T indicates QGP formation. Source: [22].

of the jets will be similar to jets observed in p-p collisions while the second jet will be quenched. This is a result of the parton forming the first jet going directly to vacuum and the other parton going through the hot dense matter - QGP - which results in energy loss and therefore the jet quenching. Observations of dijets, where one of them is quenched are now considered a strong indication of QGP formation. This situation can be seen in Fig. 1.9, where a peak at 0 deg is an indication that a dijet has formed, while the peak at 180 deg is observable in p-p and d-Au collisions only. The lower height of the peak at 180 deg is due to CNM effects.

Since jet quenching is not the main focus of this thesis, only this brief summary is included. For further details on jets and jet quenching see [24].

1.3.3 Quarkonia Production Suppression

The suppression observed in quarkonia production is a strong indication of QGP formation. The main observed signals are from the ψ states ($J/\psi, \psi'$) and the $\Upsilon(nS)$ states. Both show high level of suppression in A-A collisions compared to p-p and p-A collisions, as seen in Fig. 1.10. In peripheral collisions, the nuclear modification factor (sec. 1.5) is very close to 1 (no suppression), whereas in the most central collisions (large number of participants, N_{part}), the $R_{AA} \sim 0.2$. As mentioned in sec. 1.3, the idea of quarkonium production suppression was proposed in 1986 by Matsui and Satz and has since become one of the main focuses of modern experiments. It provides the possibility to determine the (approximate) temperature of the medium created after the high energy collision. By measuring the yield of different quarko-

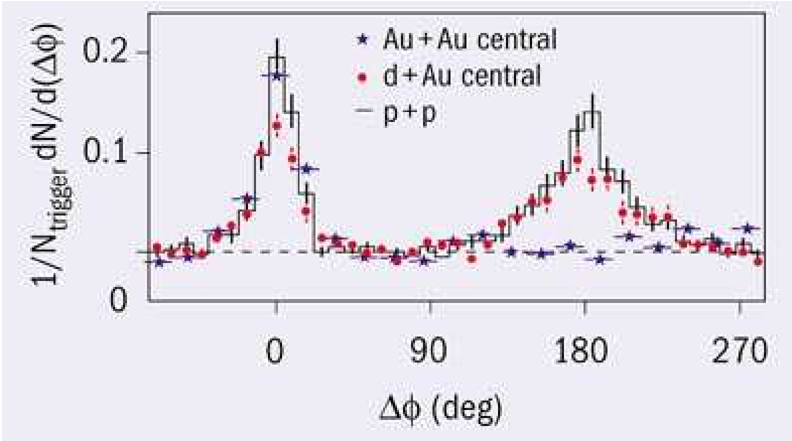

Figure 1.9: STAR measurement of hadron count distribution. One peak at 0 deg is observed in all types of collisions - indication that a dijet has formed. The jet quenching is observed as a lack of second peak (at 180 deg) in Au-Au collisions. In p-p and d-Au collisions, the second peak is clearly observable, indicating only mild energy losses due to CNM effects. Source: [23].

nia, the temperature interval can be determined as different quarkonia dissolve at different temperatures (the lower the binding energy/larger distance between the quark and the antiquark, the lower the temperature needed), creating a quarkonium thermometer (see sec. 1.3, Fig. 1.6).

The main focus of this thesis is on the $\Upsilon(nS)$ production suppression in QGP. The theoretical background is the concern of the following chapter 2, the results are shown in chapters 3 and 5.

1.4 QCD Phase Diagram

The QCD phase diagram is a plot of matter temperature against its baryon chemical potential. The calculations of this phase diagram are done in the lattice QCD framework. There is a great need for experimental confirmation of these results, especially finding the location of the critical point in the QCD phase diagram and thus proving its existence, although some significant progress has been made ([27], [28]). The QCD phase diagram can be seen in Fig. 1.11, showing the RHIC Beam Energy Scan conducted at STAR, the critical point position and the phase transition lines. Very interesting are the observations of phase transitions. Prior to reaching the critical point, these transitions are of the first order, while beyond the critical point, these transitions appear to be crossover transitions - mixed first order and second order phase transitions. These observations are the results of the RHIC Beam Energy Scan (see sec. 4.1, [29]).

To obtain a QCD phase diagram, such as in Fig. 1.11, the thermodynamic variables of the matter need to be determined. Naturally, this cannot be done by any conventional means, but rather by studying probes in the QGP formed in A-A collisions.

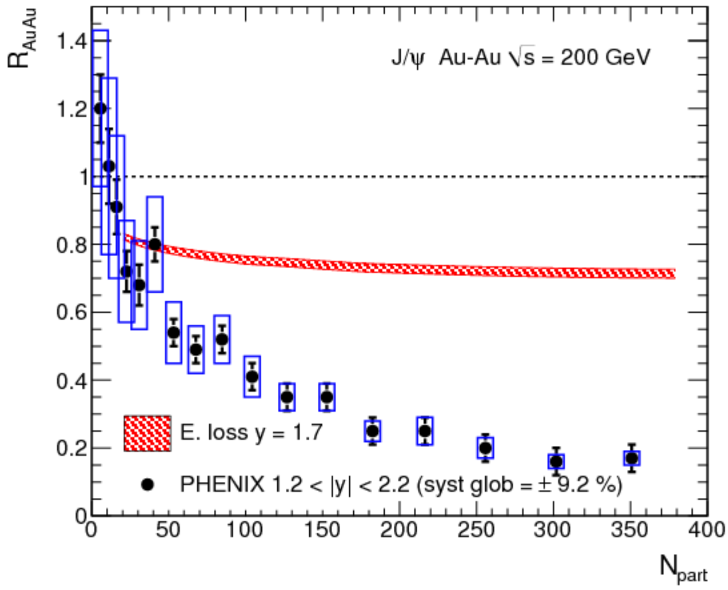

Figure 1.10: PHENIX results illustrating the J/ψ production suppression in 200 GeV Au-Au collisions. Plotted is the ratio of observed yield and measured yield from p-p collisions (see sec. 1.5) against the collision centrality. This is mainly due to the formation of the QGP in more central collisions (higher N_{part}). Some non-QGP effects are summed up by the energy loss prediction). Source: [25].

Those probes were discussed in sec. 1.3.

1.5 Nuclear Modification Factor

Even though the A-A collision can be viewed as separate nucleon-nucleon collisions, the measured yield of quarkonia in both cases will be different, partially due to the formation of the QGP. To measure the effect that the QGP has on the quarkonia production a variable called nuclear modification factor, R_{AA}, is introduced. It is the ratio of the measured A-A yield and the measured p-p yield multiplied by mean number of collisions, or:

$$R_{AA} = \frac{\frac{\mathrm{d}^2 N_{AA}}{\mathrm{d}p_T \mathrm{d}y}}{\langle N_{coll} \rangle \times \frac{\mathrm{d}^2 N_{pp}}{\mathrm{d}p_T \mathrm{d}y}} \tag{1.2}$$

This factor then includes all effects the nuclear matter (hot and cold) has. Additional measurements are required to separate effects caused by the hot nuclear matter

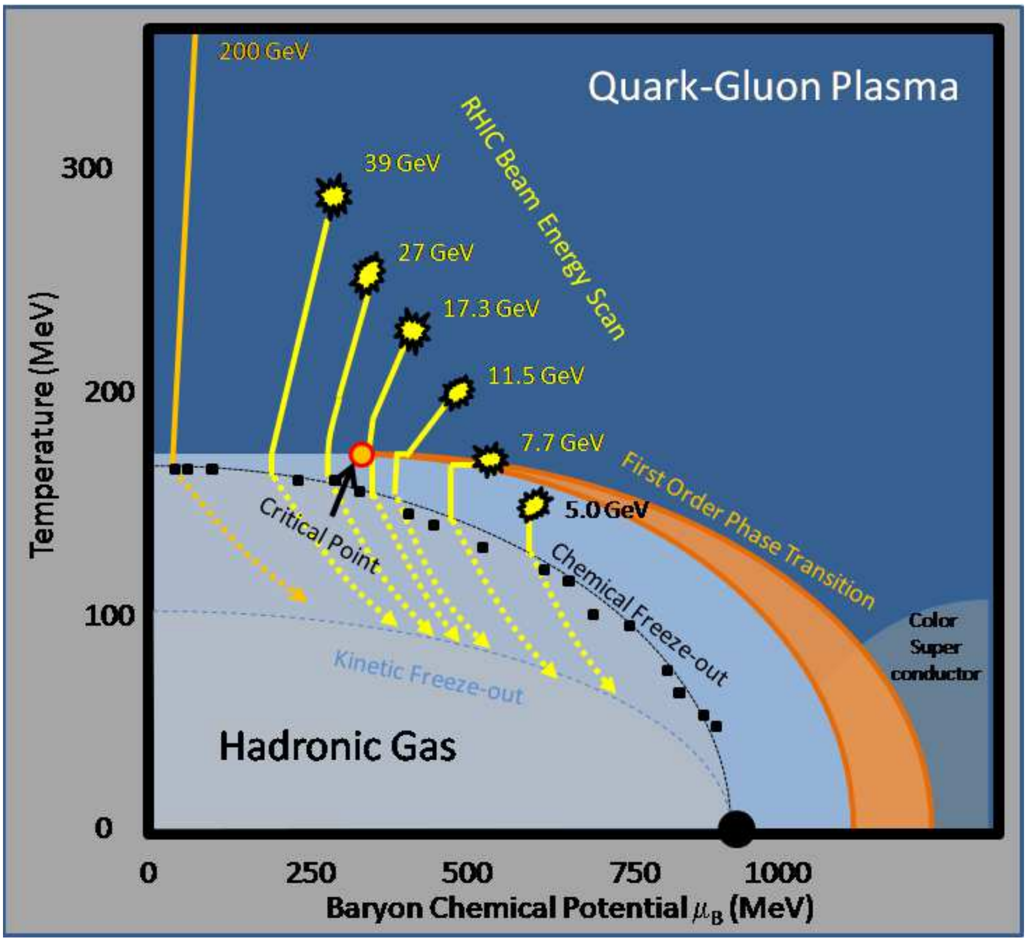

Figure 1.11: QCD phase diagram, plot of temperature against baryon chemical potential. The phase transition and freeze-out lines are shown, as well as the critical point, different states of matter and position of the RHIC Beam Energy Scan measurements. Source: [26].

from the cold nuclear matter (CNM) effects such as shadowing, anti-shadowing, hydrodynamics, recombination,... To determine those non-QGP effect, A-A collision results are compared to those in p/d-A collisions (characterized by R_{pA}/R_{dA}, defined similarly as R_{AA}, 1.2) where many of the above-mentioned effects are present, but - as far as it is known - no QGP is formed. Even though recombination is a CNM effect, it is only present in events, where hot nuclear matter has formed.

An example of the R_{AA} measurement can be seen in Fig. 1.12, showing that with increasing centrality (larger N_{part}) of the Au-Au collisions the production of $\Upsilon(1S + 2S + 3S)$ (left) is more and more suppressed. The suppression of the total $\Upsilon(1S)$ production (right) is due to the suppression of higher states (reduced feed down), because the energy in RHIC Au-Au collisions is not high enough for $\Upsilon(1S)$ to dissolve.

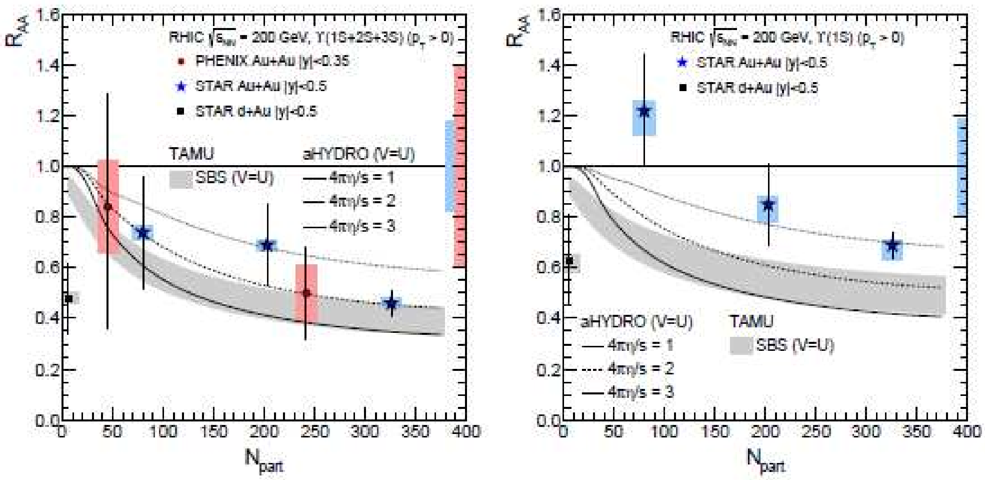

Figure 1.12: An example of RHIC measurement of R_{AA} dependence on the number of participants, compared to different theoretical models. Source: [30]

Chapter 2

Quarkonia

Quarkonia are very specific and interesting particles. Both c and b quarks were first observed in quarkonium states. They are bound states of a quark and a corresponding antiquark (naming and classification in sec. 2.1). There are two quakonium families (charmonium and bottomonium), each containing a few ground states and many excited states. Certain quarkonium states serve as a probe in the QGP (sec. 2.2). To understand some of the QGP effects, the formation of the quarkonia (sec. 2.3) needs to be studied as well. The main focus of this thesis is on the bottomonium family (sec. 2.4) and specifically on the $\Upsilon(nS)$ meson.

2.1 General Classification

Quarkonia are bound states of a quark and its own antiquark. Usually, only $c\bar{c}$ and $b\bar{b}$ mesons are called quarkonia - charmonia and bottomonia respectively. Bound states of $u\bar{u}$ and $d\bar{d}$ are called π^0 meson - ground state and ρ^0 meson - excited state, while the bound $s\bar{s}$ state is called the ϕ^0 meson. All these particles are then observable in the dilepton (usually dielectron and dimuon) invariant mass spectrum as peaks at certain mass values. An example of the dimuon invariant mass spectrum can be seen in Fig. 2.1, where the peaks are clearly visible. The only exception is the π^0 peak, since the π^0 to dimuons decay channel is blocked, because the mass of π^0 is much lower than the mass of a $\mu^+\mu^-$ pair.

Quarkonia can be classified by their wave function type as well. This divides the quarkonium families into two branches - the S states (ψ and Υ states) and the P states (χ_c and χ_b states). The P states are much less abundant in detected events and are somewhat exotic particles. Nevertheless some P states measurements are still conducted mainly to measure the feed down of the lower energy states.

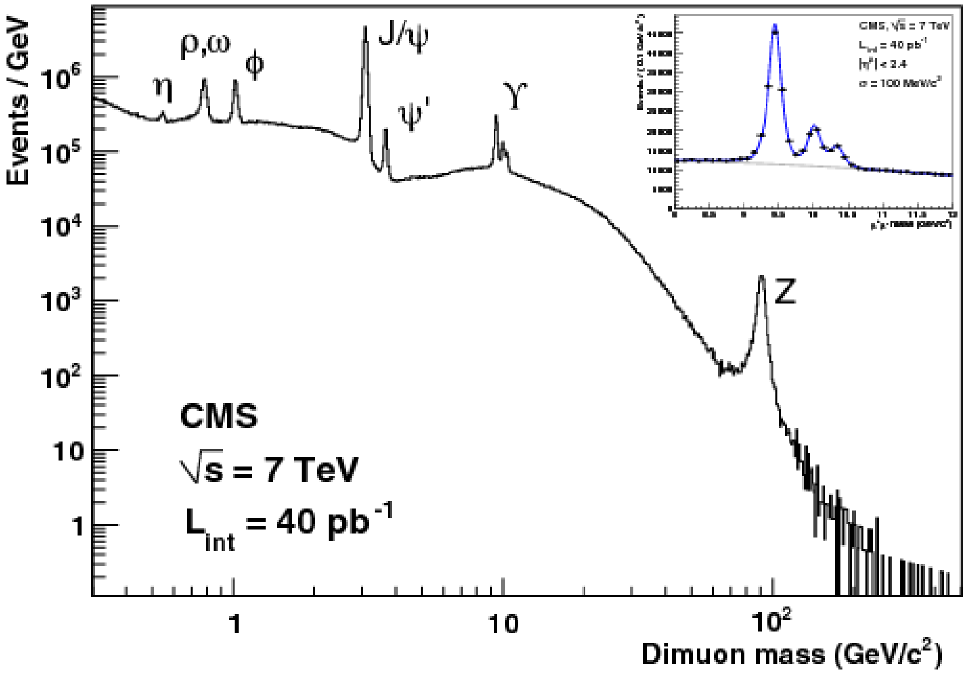

Figure 2.1: CMS measurement of dimuon invariant mass spectrum. Visible peaks indicate existence of a particle of specific mass equal to the value of the middle of the peak. The zoomed-in window shows the $\Upsilon(nS)$ system. Source: [31].

2.2 QGP Probe

As mentioned in subsection 1.3.3, the suppression of heavy quarkonia production is one of the main indications that the QGP has formed during the event. First proposed in 1986 by Matsui and Satz, [17], the production of quarkonia is suppressed in hot nuclear matter, because of the phenomenon known as the Debye screening. The color-charged particle polarizes the hot nuclear matter (which is possible thanks to the deconfined color-charged partons) which in return weakens the color field of the heavy quark (component of the quarkonium). Provided the temperature is high enough, the two heavy quarks then cannot "see" each other and the quarkonium ceases to exist. The presence of those free color charges is granted by an important property of the strong interaction - the asymptotic freedom - which is a result of the α_s constant's natural tendency to decrease at high energies (and therefore temperatures, see sec. 1.3). It is important to note that quarkonia usually form before the QPG formation. In a heavy-ion collision, the quarkonium goes through four stages of evolution. The formation (sec. 2.3), life in vacuum, the CNM-only phase, in which the quarkonium interacts with the scattered nuclear matter, and the QGP phase (where both QGP and CNM effects are present). During its brief existence in vacuum, the $q\bar{q}$ pair is described by a potential in the form of:

$$V(r, T = 0) = -\frac{4}{3}\frac{\alpha_s(r)}{r} + \sigma r, \tag{2.1}$$

where the first term is Coulombic and the second term is a string term characterized by a string tension constant σ. The Coulombic term is dominant at short distances and is responsible for the asymptotic freedom. This means that when the quarks get very close, they almost behave like free particles. The string term is responsible for another phenomenon - the quark confinement. As the quark and the antiquark are pulled further away from each other, the bond does not weaken, but strengthens to the point where it is more energetically favorable to create another $q\bar{q}$ pair out of the vacuum to form two mesons and reduce the quark-antiquark distance. This is similar to a situation where two ends of a string are pulled further and further apart to the point where the string snaps and splits into two shorter strings.

During the CNM-only phase, still before the QGP has formed, the quarkonium interacts with the scattered nuclear matter and this leads to effects such as shadowing, anti-shadowing and nuclear absorption. These effects are not observed in p-p collisions but are observable in p-A, d-A and A-A collisions. These effects persist during the QGP phase (which is observable in high-energy A-A collisions only) in addition to the hot nuclear matter effects, such as the elliptic flow and jet quenching (described in sec. 1.3). The quarkonium is described by a modified version of the potential (eq. 2.1) in the QGP. This potential accounts for non-zero temperature and color screening in the medium:

$$V(r,T) = -\frac{\alpha_{eff}}{r}\exp(-\frac{r}{\lambda_D(T)}) + \sigma\lambda_D(T)[1-\exp(-\frac{r}{\lambda_D(T)})], \tag{2.2}$$

where α_{eff} and σ are constants and $\lambda_D(T)$ is the Debye screening length. It is a distance, outside of which the color charge of the heavy quark is screened. This means that if the heavy quarks are further apart than the Debye screening length, they cannot "see" each other and the quarkonium therefore cannot exist. The Debye screening length can be determined from this equation:

$$\lambda_D(T) = \frac{1}{\sqrt{\frac{N_c}{3}\frac{N_f}{6}g^2 T}}, \tag{2.3}$$

where N_c and N_f are the degrees of color and flavor freedom respectively and $g^2 = 4\pi\alpha_{eff}$. The Debye screening length decreases with increasing temperature, meaning that at high temperatures the string term in eq. 2.2 (responsible for quark confinement) diminishes. More information about these processes can be seen in [17], [32].

The main idea behind the quarkonia production suppression in the QGP measurements is that they provide a way to determine the temperature of the QGP by observing which quarkonium states are suppressed and which are not. This is possible, because all quarkonia have different radii and therefore dissolve at different temperatures. In reality, we observe near 100% suppression of $\Upsilon(2S)$ and $\Upsilon(3S)$ states in central collisions at RHIC and LHC energies, but no direct suppression of the $\Upsilon(1S)$ meson. Recent results are discussed in chapter 3.

2.3 Formation

Because of their high mass, quarkonia are formed almost exclusively during the hard scattering at the beginning of the collisions. This is true especially for bottomonia - their mass is more than three times as high as the charmonium mass - and this feature is very important for the calculation of the suppression in the QGP. The main process for the initial $q\bar{q}$ pair formation is the gluon fusion. Charmonia can form in a mass interval between $m_{c\bar{c}} < m_{\eta_c} \leq m_{charm} < 2m_{D^0}$, where $m_{c\bar{c}} = 2m_c = 2.6$ GeV/c^2 is the mass of a charm-anticharm pair, $m_{\eta_c} = 3.0$ GeV/c^2 is the mass of the $\eta_c(1S)$ meson, the ground state of the charmonium family and $2m_{D^0} = 3.8$ GeV/c^2 is the open charm threshold, the mass of two D^0 mesons, the lightest particles containing the c quark. The same holds for bottomonia: $m_{b\bar{b}} < m_{\eta_b} \leq m_{bottom} < 2m_{B^0}$, where $m_{b\bar{b}} = 2m_b = 8.4$ GeV/c^2 is the mass of a bottom-antibottom pair, $m_{\eta_b} = 9.4$ GeV/c^2 is the mass of the $\eta_b(1S)$ particle, which is the ground state of the bottomonium family and $2m_{B^0} = 10.6$ GeV/c^2 is the mass of two B^0 mesons, the lightest particles containing the b quark - the open beauty threshold. All masses were taken from the Particle Data Group, [33]. Theoretically, charmonia and bottomonia with masses above the respective open flavor thresholds do exist. However, since it is more energetically favorable to create a D or B meson pair when above this threshold, the production of these highly excited states is severely suppressed (for more on these resonances see [34]).

The process of quarkonia formation is not yet completely described within the QCD framework, partially because even though the formation of a quarkonium can be calculated using perturbation QCD, the evolution of that quarkonium is a soft process, so pQCD cannot be used. However, several theoretical models do exist and are discussed in the following subsections (2.3.1, 2.3.2, 2.3.3). For more detailed information about these models see [30].

2.3.1 Color Evaporation Model

According to [30], the simplest model describing quarkonium production is the Color Evaporation Model (CEM). This model predicts that the color state of a given $q\bar{q}$ pair is completely unrelated to the color state of the quarkonium at hadronization, effectively meaning that any $q\bar{q}$ pair can form a quarkonium. This is realized by an emission of low energy gluons. The probability that a given quarkonium state is obtained is then characterized by a statistical factor $F_Q = 1/9 \times (2J_Q + 1)/\Sigma_i(2J_i + 1)$, where J_Q is the spin of the quarkonium and i is the index running over all possible quarkonium states. This can be written as:

$$\sigma_Q^{(N)LO} = F_Q \int_{m_{q\bar{q}}}^{m_{OF}} \frac{\mathrm{d}\sigma_{q\bar{q}}^{(N)LO}}{\mathrm{d}m_{q\bar{q}}} \mathrm{d}m_{q\bar{q}}. \tag{2.4}$$

This model offers phenomenology fairly consistent with measured data, but cannot be used for polarization predictions.

2.3.2 Color Singlet Model

The exact opposite assumption is the basis for the second simplest model for quarkonia production - the Color Singlet Model (CSM). The CSM assumes that the quantum state (spin, color) of the $q\bar{q}$ pair does not evolve between the formation and the hadronization. This model also assumes that the quarkonia are non-relativistic (which seems to be a valid assumption). The CSM is nearly fully predictive, but suffers from phenomenological issues.

2.3.3 Color Octet Model

The Color Octet Model (COM) was developed in the non-relativistic QCD (NRQCD) and is now considered a part of it along with the CSM. This model is more successful in cross section predictions than the CSM. On the other hand, the COM predicts strong transverse polarization which has not been observed.

2.4 Bottomonium Family

Bottomonium family is the name for the set of all $b\bar{b}$ mesons. The family consists of ground states ($\eta_b(1S)$, $\Upsilon(1S)$) and many resonances (excited states). The most notable are the S states: $\Upsilon(2S)$, $\Upsilon(3S)$ and the P states: $\chi_b(1P)$, $\chi_b(2P)$ and $\chi_b(3P)$, the first particle discovered at the LHC, [35]. Other states are rather exotic and not studied extensively. Higher excited states - for example $\Upsilon(4S)$ - are possible, but their masses lie above the open beauty threshold (see sec. 2.3) and therefore are very rarely observable, because the creation of two B mesons is then more energetically favorable. The bottomonium family is shown in Fig. 2.2, along with deexcitation lines - the feed down channels. Feed down from resonances is very important source of the lower states (especially $\Upsilon(1S)$). As seen in 2.3, at high p_T, more than half of the observed $\Upsilon(1S)$ mesons are a result of a feed down from resonances (mainly $\Upsilon(2S+3S)$ and $\chi_b(1P)$ mesons). Direct production is always the main source of a given $\Upsilon(nS)$ meson and the most important feed down source is the corresponding $\chi_b(nP)$ meson.

2.4.1 $\Upsilon(nS)$ Meson

There are 3 $\Upsilon(nS)$ mesons below the open beauty threshold. Although some higher excited S states do exist, their production is very rare, because two B mesons are more likely to be created as this process is less energetically demanding. For all three mesons $J^{PC} = 1^{--}$. Other $\Upsilon(nS)$ properties are summarized in Tab. 2.1.

All values in Tab. 2.1 were taken from Particle Data Group, [33], except for τ values which were approximated using

$$\tau = \frac{\hbar}{\Gamma}. \tag{2.5}$$

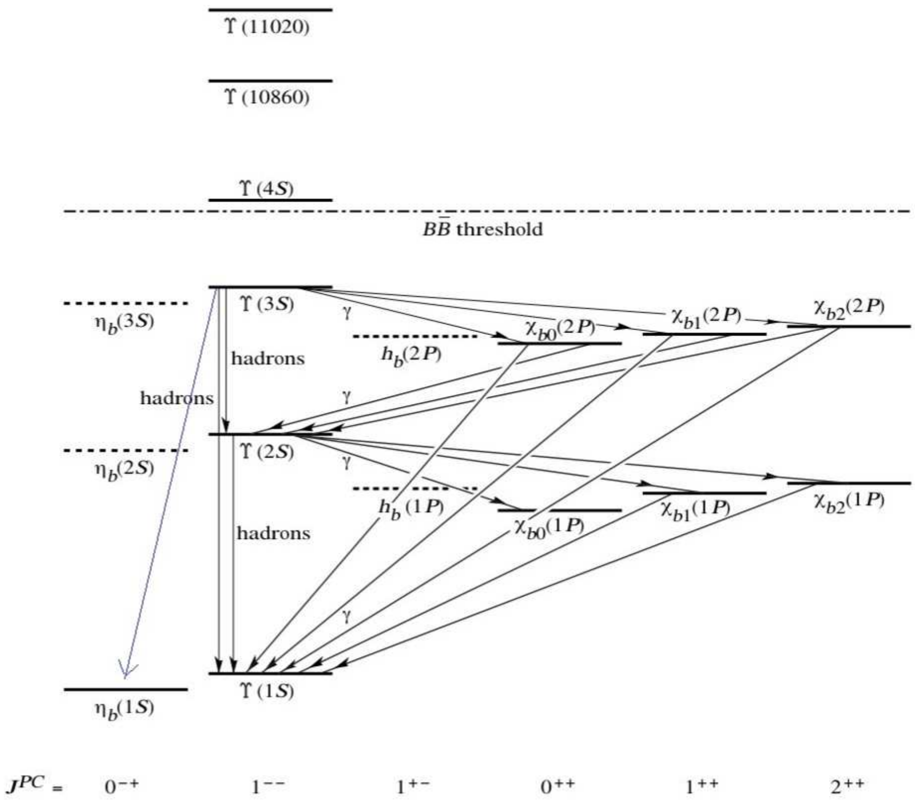

Figure 2.2: The bottomonium family, ascending with increasing mass. All known $b\bar{b}$ mesons are shown, with the exception of $\chi_b(3P)$, along with deexcitation lines - feed down channels. The open beauty ($B\bar{B}$) threshold is marked as well. Source: [36].

n [-]	mc^2 [MeV]	Γ [keV]	τ [10^{-20} s]	MDC
1	9460.30 ± 0.26	54.02 ± 1.25	1.22	leptons
2	10023.26 ± 0.31	31.98 ± 2.63	2.06	family, leptons
3	10355.20 ± 0.50	20.32 ± 1.85	3.24	family, leptons

Table 2.1: Values of some basic properties of $\Upsilon(nS)$ mesons, mc^2 - invariant mass, Γ - decay width, τ - approximate mean lifetime, MDC - main decay channels.

2.4.2 Discovery

The $\Upsilon(1S)$ meson was first observed in 1977 at Fermilab by an experimental team lead by Leon Lederman. This team observed a strong resonance in dimuon invariant mass spectrum at $m_\Upsilon = 9.5$ GeV$/c^2$ measured in $\sqrt{s_{NN}} = 400$ GeV p-A collisions on fixed Pt and Cu targets. After excluding other possibilities (eg. apparatus bias), this result was interpreted as a new particle. The original picture with a visible peak at 9.5 GeV in the dimuon invariant mass spectrum can be seen in 2.4 and the details of the discovery can be seen in [37].

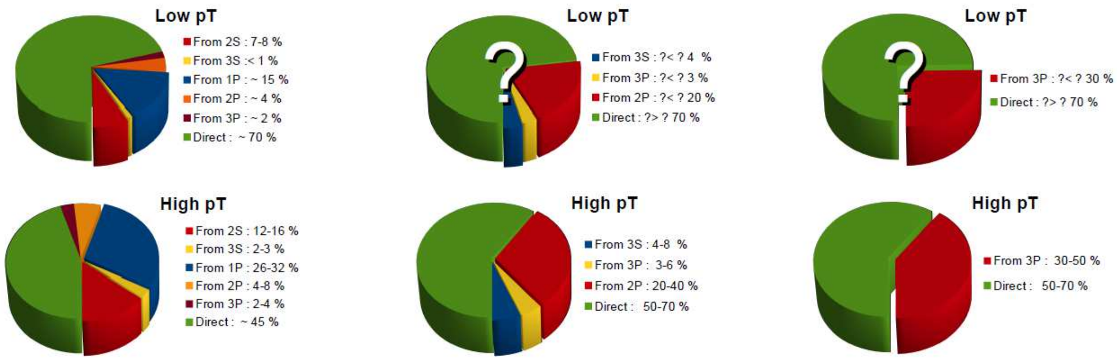

(a) $\Upsilon(1S)$ (b) $\Upsilon(2S)$ (c) $\Upsilon(3S)$

Figure 2.3: The percentages of the total yield for different sources of the $\Upsilon(nS)$ meson - the ratio of feed down from higher states. Direct production fraction is marked green. Also categorized by p_T. Data derived from primarly from LHC measurements. Source: [30].

2.4.3 Advantages of $\Upsilon(nS)$

There are certain properties of $\Upsilon(nS)$ mesons that make them a more suitable probe in the QGP than ψ states. First and most important, three $\Upsilon(nS)$ mesons exist under the open beauty threshold. Only two ψ mesons exist under the open charm threshold. Therefore, the $\Upsilon(nS)$ measurements provide finer temperature scaling of the QGP. Moreover, the Υ states are very different in binding energy, and therefore allow the probing of a wider range of QGP temperature. The $\Upsilon(nS)$ states exhibit closer relative abundance as well. The ratio $\Upsilon(1S)$:$\Upsilon(2S)$:$\Upsilon(3S)$ is 7:2:1, which leads to easier observability during their suppression in the QGP than the ψ states (J/ψ:$\psi' = 50$:1, [30]). Another advantage of Υ over ψ mesons is their significantly larger mass. Not only are the relativistic effects due to Υ mesons' motion even less significant than in the charmonium family (to the point of negligibility), but this also means that the Υ mesons decay practically at rest, leading to easily detectable decay products (leptons). Those leptons are highly specific, as they scatter at very large mutual angles - close to π - and are very energetic. Furthermore, the high Υ mass assures no additional production after the hard scattering part of the event. The final advantage is the absence of any beauty feed down in Υ production, compared to significant feed down from decaying b quarks for charmonia, especially at higher energies.

On the other hand, several disadvantages are present in Υ production measurements. One of them is the higher complexity of the bottomonium family, as shown in sec. 2.4, and thus the more complex feed down from resonances. This leads to theoretical and practical difficulties, especially the need for a higher detector resolution. Another one is the total abundance, which is much lower for Υ mesons compared to ψ mesons. This is especially significant for lower (RHIC) energies, while at LHC energies the production ratio is around 1:200 in favor of the ψ mesons, which is satisfactory, [30].

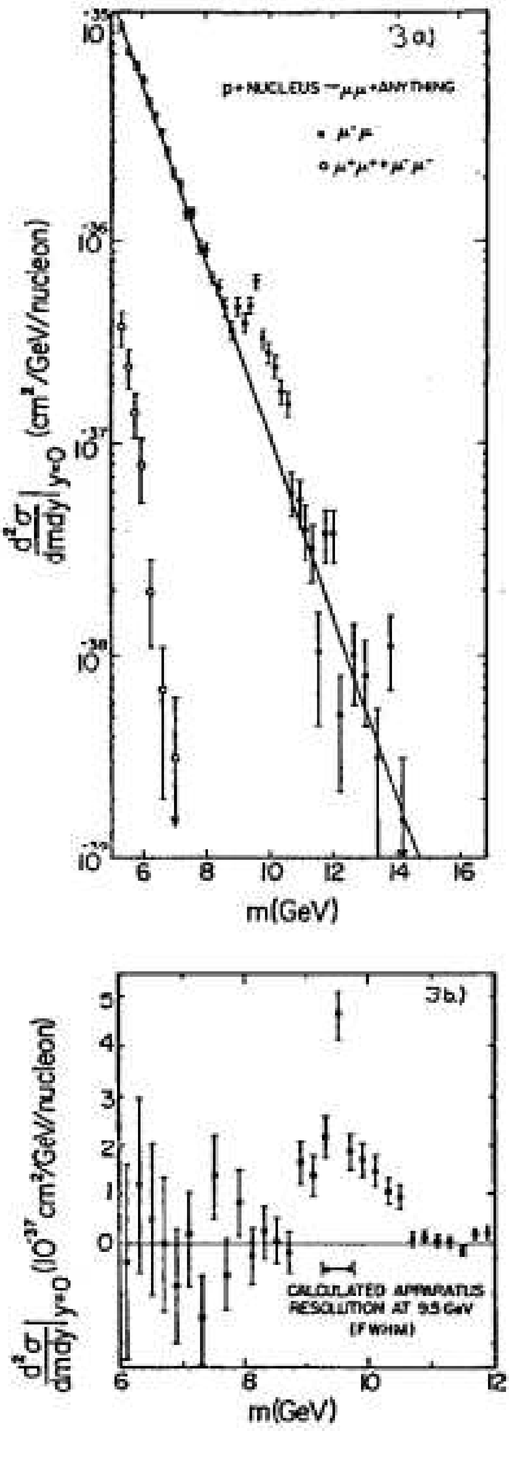

Figure 2.4: The dimuon invariant mass spectrum with a peak visible at 9.5 GeV as published in the original paper, [37]. Top: before background subtraction, bottom: after background subtraction.

Chapter 3

RHIC and LHC Results

In present days, quarkonia production is measured at two particle accelerators. The first one is the Relativistic Heavy-Ion Collider (RHIC), located in the U.S. and its experiments PHENIX (sec. 3.1) and mainly STAR (sec. 3.2). The other one is the Large Hadron Collider (LHC) at CERN under the Swiss-French border. Especially the ALICE (sec. 3.3), ATLAS (sec. 3.4) and CMS (sec. 3.5) collaborations at the LHC are conducting quarkonia-related measurements.

3.1 PHENIX

The PHENIX collaboration has published their results of $\Upsilon(1S+2S+3S)$ in a 2012 paper, [38]. The collaboration focused on Υ production in p-p and d-Au collisions with main objective to measure the CNM effects on the production. The PHENIX detector provides measurements in far forward and far backward rapidities.

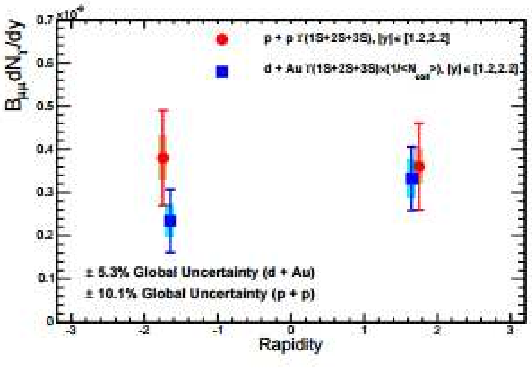

Figure 3.1: PHENIX results of $\Upsilon(1S + 2S + 3S)$ yield dependence on rapidity. Red points represent the yield in p-p collisions and blue ones are the yield in d-Au collisions scaled by the average number of participants. Source: [38].

As seen in Fig. 3.1, the scaled yield in forward rapidity is nearly identical ($R_{dA} =$

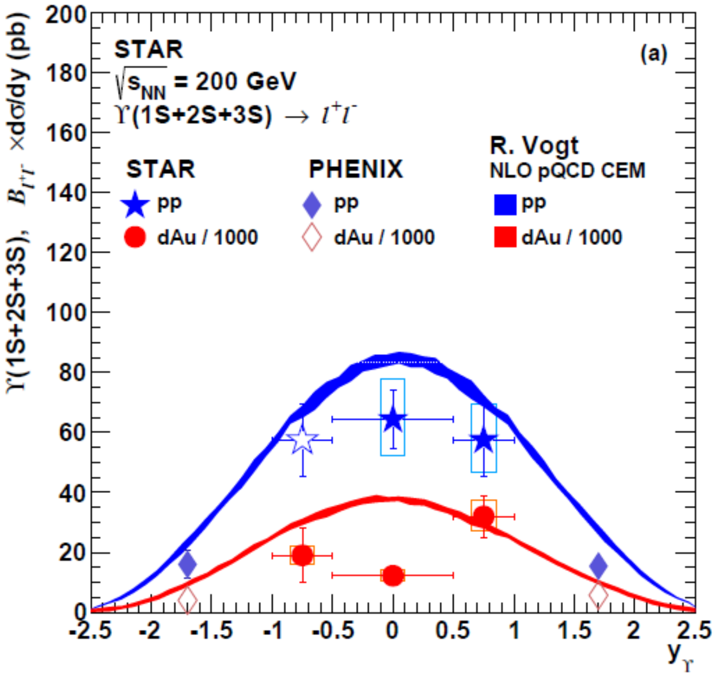

Figure 3.2: The combined $\Upsilon(1S+2S+3S)$ yield in p-p and d-Au 200 GeV collisions from dilepton channels as a function of rapidity as measured by STAR. The d-Au yields are scaled by 1/1000 to fit in the graph. Data compared to PHENIX results and CEM predictions (2.3.1). Source: [39].

$0.91 \pm 0.33(stat) \pm 0.16(syst)$) while in backward rapidities, a certain level of suppresion is observed. This corresponds to $R_{dA} = 0.62 \pm 0.26(stat) \pm 0.13(syst)$. Because of the large uncertainties, these results are not very conclusive and further measurements need to be conducted.

3.2 STAR

The STAR detector covers the mid-rapidity section, complementing the PHENIX detector. At STAR, several types of collisions were studied in order to determine the effect each system has on the quarkonia production. First, the p-p and d-Au collisions were measured in order to determine the non-suppressed yield and the CNM effects. These results can be seen in Fig. 3.2, the main observation being that theoretical prediction tends to overestimate the obtained data.

STAR results of R_{AA} indicate strong suppression in combined $\Upsilon(1S+2S+3S)$ production in central Au-Au and U-U collisions, consistent with theoretical prediction and CMS results. These results can be seen in Fig. 3.3. The conclusion of these results is that the higher $\Upsilon(nS)$ states are highly suppressed in the QGP, but the $\Upsilon(1S)$ state is not. The observed value of $R_{AA}^{1S} \simeq 0.6$ is a result of suppressed feed down from higher states and not of the suppressed direct production of $\Upsilon(1S)$.

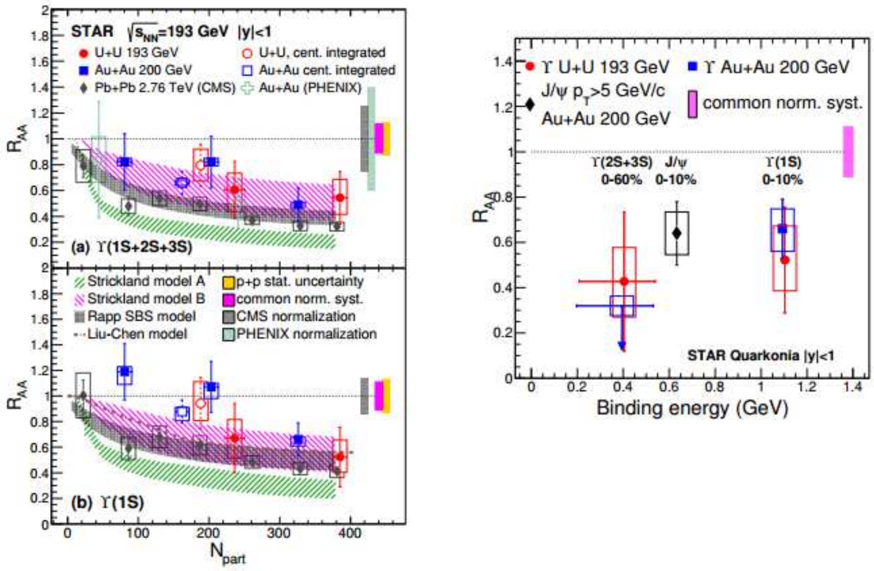

Figure 3.3: Left: (a) STAR R_{AA} measurement in 200 GeV Au-Au (blue) and 193 GeV U-U collisions (red) as a function of the number of participants for combined $\Upsilon(1S + 2S + 3S)$. Compared to CMS Pb-Pb (black) and PHENIX Au-Au (silver) results and theoretical predictions. (b) Same R_{AA} measurement for $\Upsilon(1S)$ only, compared to theoretical predictions, no PHENIX data available. Right: Comparison of suppression of different quarkonium states as measured by STAR. Source: [40].

Future measurements should include the R_{AA} on p_T dependence as these results are lacking.

3.3 ALICE

The LHC collides lead nuclei instead of gold or uranium as is the case at RHIC. The ALICE experiment published its recent results from 2.76 TeV Pb-Pb collisions in 2014, [41]. As seen in Fig. 3.4, the theoretical model underestimates the suppression ($R_{AA} = 0.30 \pm 0.05(stat) \pm 0.04(syst)$ in the most central collisions). Overall, the results are very similar to STAR results (sec. 3.2), both showing high level of suppression in central A-A collisions. However this comparison is not to be taken conclusively as it is important to point out that ALICE measures in far rapidities whereas STAR covers the mid-rapidity section.

While theoretical models overestimate the measured data, but generally follow the observed trend (often indication of a systematic error) for R_{AA} dependence on N_{part}, the measurements of R_{AA} dependence on rapidity show a discrepancy between data and theory, as evident in Fig. 3.5, bottom.

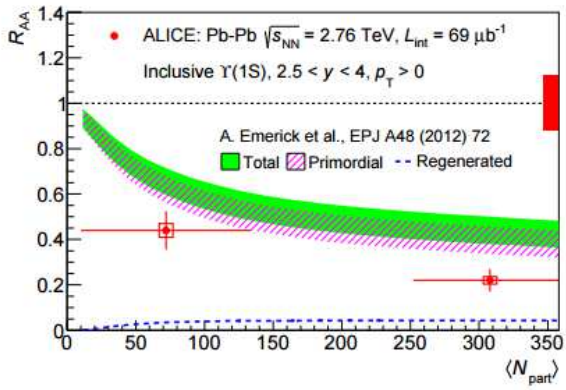

Figure 3.4: ALICE R_{AA} measurement as a function of the average number of participants in forward rapidity, 2.76 TeV Pb-Pb collisions . Data are compared to theoretical prediction. Source: [41].

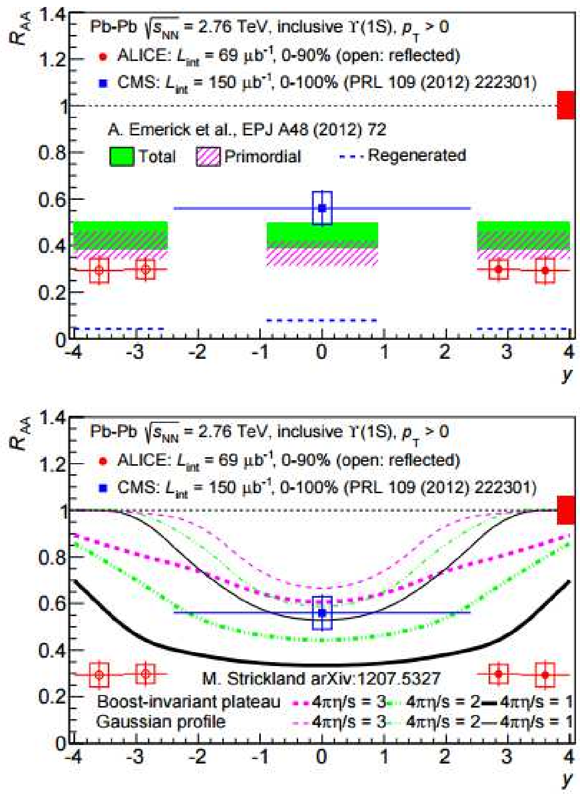

Figure 3.5: ALICE (red, full) results of R_{AA} dependence on rapidity for $\Upsilon(1S)$ in 2.76 TeV Pb-Pb collisions compared to theoretical predictions. CMS results (blue) included. Source: [41].

3.4 ATLAS

The ATLAS collaboration presented their preliminary results at the 2015 QM conference ([42]). The results included the measurements of the $\Upsilon(nS)$ mass range in the dimuon invariant mass spectrum in 2.76 TeV p-p (Fig. 3.6) and 5.02 TeV p-Pb (Fig. 3.7) collisions and R_{pPb} measurement (Fig. 3.8)for the $\Upsilon(1S)$ meson. The R_{pPb} appears constant throughout the centrality range, but the result is somewhat open to interpretation (also inconsistent with STAR results, [39]).

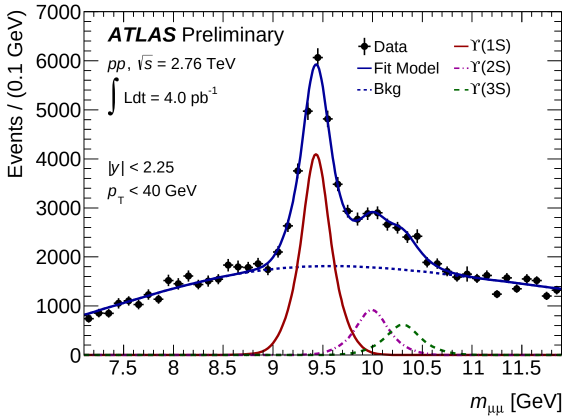

Figure 3.6: $\Upsilon(nS)$ invariant mass spectrum as measured by ATLAS in 2.76 TeV p-p collisions. Source: [42].

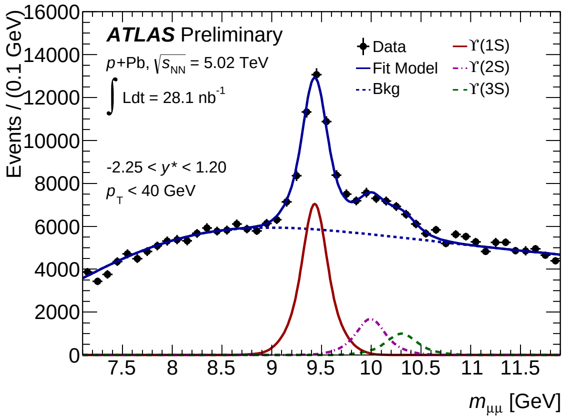

Figure 3.7: ATLAS measurement of $\Upsilon(nS)$ invariant mass spectrum in 5.02 TeV p-Pb collisions. Source: [42].

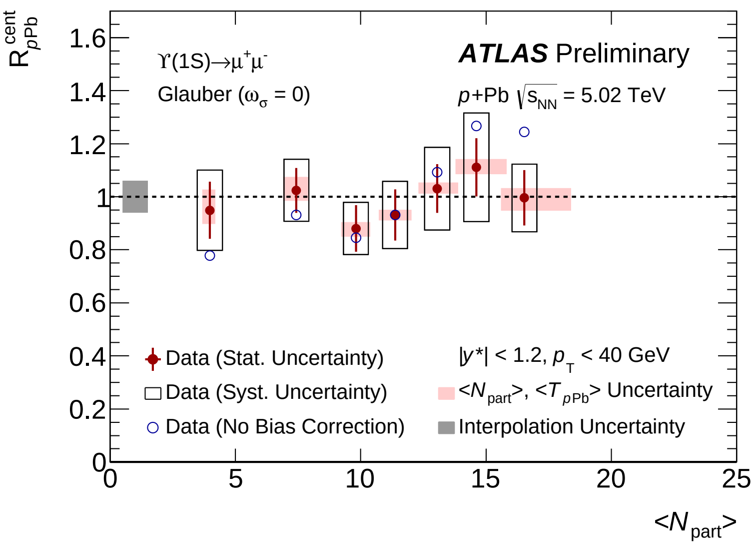

Figure 3.8: ATLAS measurement of R_{pPb} as a function of collision centrality in 5.02 TeV p-Pb collisions. Source: [42].

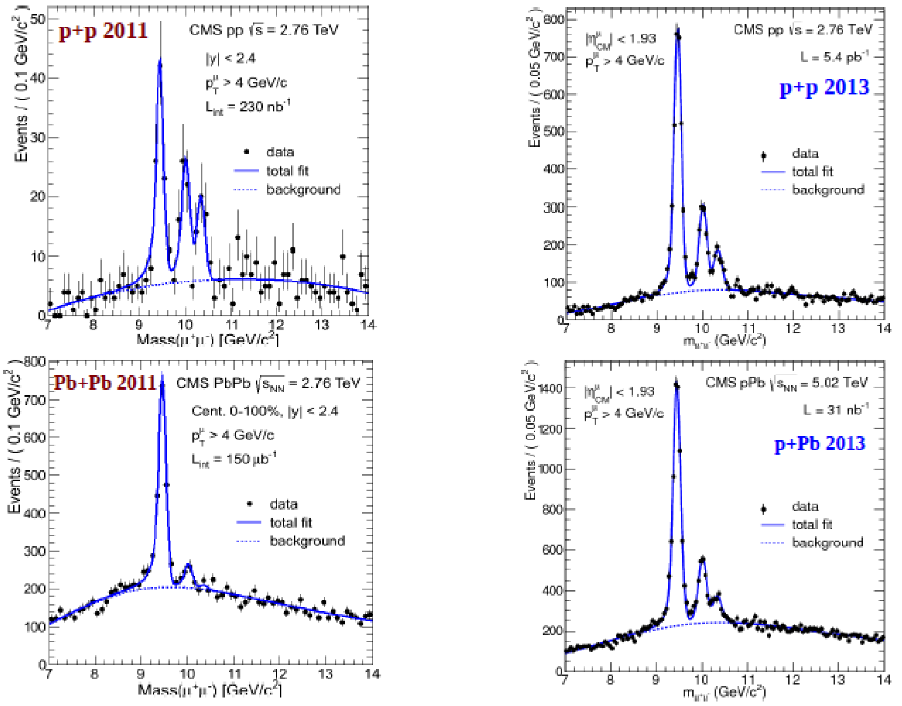

Figure 3.9: left: 2011 (left) and 2013 (right) CMS results of $\Upsilon(nS)$ invariant mass spectrum measurements in p-p, p-Pb and Pb-Pb collisions. Source: [43].

3.5 CMS

The CMS collaboration presented their $\Upsilon(nS)$ measurements results at the 2015 QM conference ([44]). The published results include the $\Upsilon(nS)$ invariant mass spectra in p-p, p-Pb and Pb-Pb collisions. These results can be seen in Fig. 3.9 and Fig.3.10.

It can be seen (Fig. 3.9) that the $\Upsilon(2S)$ and $\Upsilon(3S)$ states are slightly suppressed in p-Pb collision in comparison to p-p collisions and these states are heavily suppressed in Pb-Pb collisions (especially $\Upsilon(3S)$). The difference of p-p and Pb-Pb results is clearly observable in 3.10, with heavy suppression of higher Υ states and lower suppression of the $\Upsilon(1S)$ state, meaning that the QGP temperature during Pb-Pb collisions is between the temperature of $\Upsilon(1S)$ deconfinement and the $\Upsilon(2S)$ deconfinement temperature. The CMS-measured $R_{AA} = 0.43 \pm 0.03(stat) \pm 0.07(syst)$ of $\Upsilon(1S)$ production shows higher suppression at LHC energies than at RHIC energies (STAR: $R_{AA} = 0.52 \pm 0.23(stat) \pm 0.09(syst)$, [40]). The CMS R_{AA} measurement results can be seen in Fig. 3.11 and show high suppression in high-centrality collisions which is in good consistency with theoretical prediction. The suppression of $\Upsilon(1S)$ should be interpreted as a suppression of feed down from higher states, not as a suppression of the state itself.

As far as R_{AA} dependence on p_T is concerned, preliminary CMS results Fig. 3.12 indicate that theoretical models describe the $\Upsilon(1S)$ suppression well, whereas the $\Upsilon(2S)$ suppression description is questionable. Overall the data suggest no significant suppression dependence on p_T.

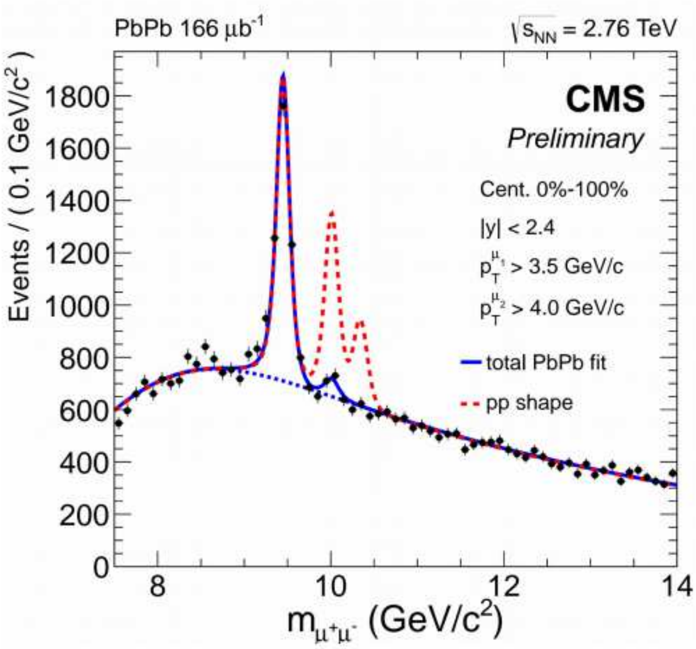

Figure 3.10: Preliminary CMS result of the dimuon invariant mass spectrum (around $\Upsilon(nS)$ mass range) in 2.76 TeV Pb-Pb collisions (mid-rapidity, all centralities), compared to p-p spectrum shape (scaled to $\Upsilon(1S)$ Pb-Pb yield). Source: [44].

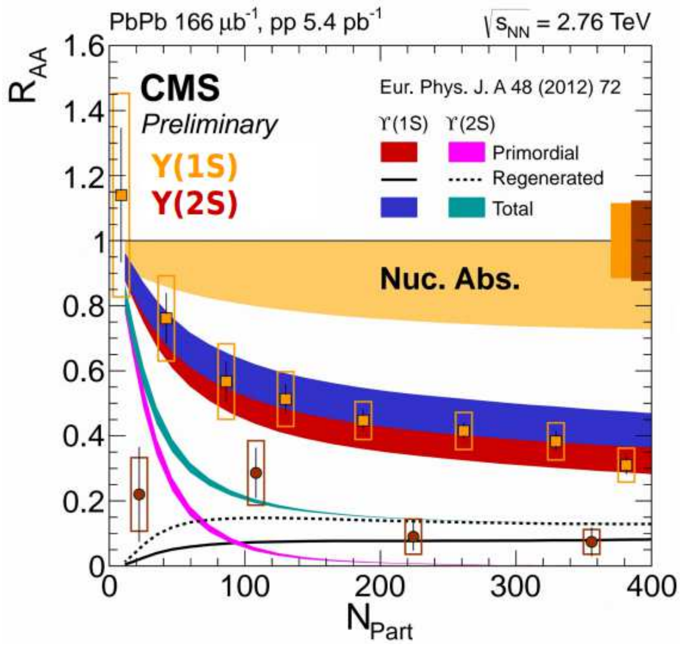

Figure 3.11: Preliminary CMS results of R_{AA} for $\Upsilon(1S)$ and $\Upsilon(2S)$ states as a function of centrality and comparison to theoretical prediction. Source: [44].

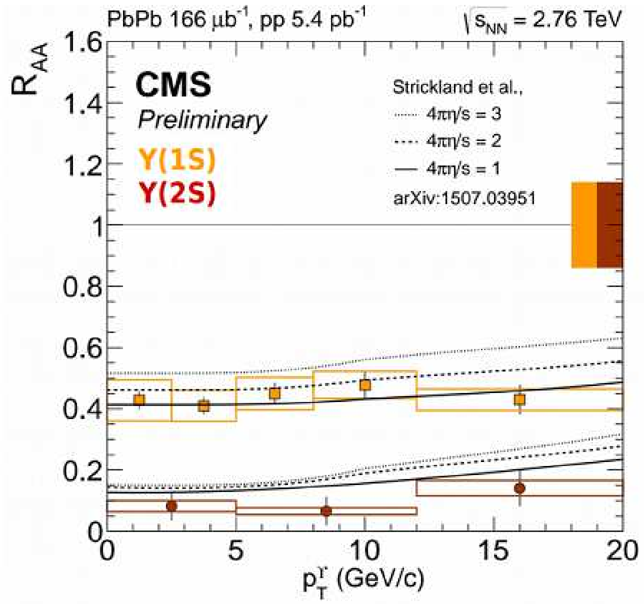

Figure 3.12: Preliminary CMS results of R_{AA} on p_T dependence for $\Upsilon(1S)$ - yellow - and $\Upsilon(2S)$ - red - compared to theoretical prediction. Source: [44].

Chapter 4

Experimental Setup

To study the conditions of the early Universe, humans have built large machines that accelerate and collide heavy nuclei. In these high energy collisions, the extreme conditions of the early Universe are re-created. One of those particle accelerators is the Relativistic Heavy Ion Collider (RHIC, sec. 4.1). To obtain experimental data, large detectors are used. These detectors consist of several components, each serving a specific purpose. The STAR detector (sec. 4.2) is one of the main detectors at RHIC and serves as the primary source of quarkonia-production-related data.

4.1 RHIC

The **R**elativistic **H**eavy **I**on **C**ollider - RHIC - is a ring particle accelerator located at the Brookhaven National Laboratory (BNL) near Upton, NY with a circumference of 3834 m. The accelerator is capable of accelerating two beams at the same time in opposite direction (there are in fact two rings) and subsequently colliding the beams at one of the six intersection points. The accelerated particles can be protons, deuterons and different heavy nuclei (copper, gold, uranium,...) which makes RHIC somewhat unique among particle accelerators. The entire process begins at the Electron Beam Ion Source, where highly charged beams are produced and accelerated by small linear accelerators. These beams are then injected into the circular Booster Synchrotron, where they are further accelerated to velocities closer to the speed of light (0.37 c) by radio frequency electromagnetic waves and subsequently injected into the Alternating Gradient Synchrotron. In the AGS the acceleration continues in a similar fashion as in the Booster. After reaching the AGS top speed (0.997 c), the beam is sent down the AGS-to-RHIC transfer line. At the end of the AtR line, the heavy ion beam is split into bunches by a magnetic switch and each bunch is injected into one of the RHIC storage rings where they are further accelerated until they reach the top speed (up to 0.99995 c). Afterwards, the particles are collided at one of the intersection points. Each of the RHIC experiments (BRAHMS, PHENIX, PHOBOS and STAR (sec. 4.2)) is located near one of the intersection points so they can collect data from the events. Only the PHENIX and STAR experiments are taking data at this time, as the BRAHMS and PHOBOS experiments finished their program. The entire accelerator complex can be seen in Fig. 4.1.

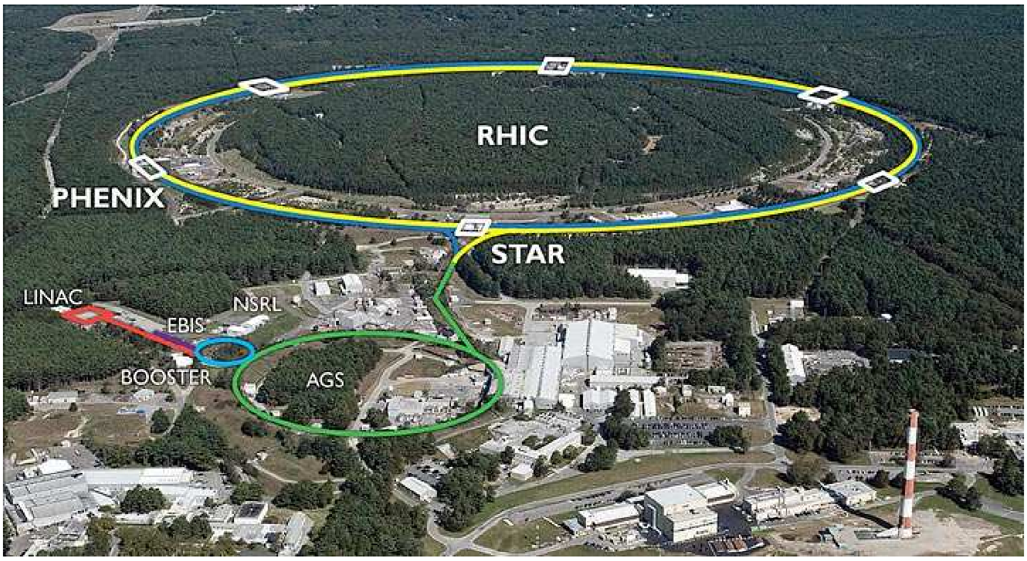

Figure 4.1: The RHIC accelerator complex at BNL. The different stages of particle acceleration are shown as well as the two main experiments - PHENIX and STAR. Source: [46]

In contrast to the LHC, which aims for the highest energies possible, RHIC is capable of colliding at different lower energies (Beam energy scan at $\sqrt{s_{NN}}$ = 7.7-200 GeV), providing measurements for various initial conditions which are essential for the completion of the QCD phase diagram (sec. 1.4). Proton-proton beams can be accelerated to energies up to $\sqrt{s_{NN}}$ =500 GeV. The future plans (BES Phase-II) for RHIC include fixed-target collisions and increased luminosity at low energies (see [29]). The construction of the world's first electron-ion collider (eRHIC), that would replace the current RHIC and would be capable of producing completely new type of events and data, is possible as well ([45]).

4.2 STAR

The **S**olenoidal **T**racker **A**t **R**HIC - STAR - is one of the main experiments at RHIC. It is a multipurpose detector capable of obtaining data from particle collisions. The design of the experiment allows the observation of interesting events at mid-rapidity (complementing the PHENIX detector which focuses on far-rapidity events). The STAR experiment is composed of a huge magnet (0.5 T solenoid), coils and several detectors such as the Time Projection Chamber (TPC, subsection 4.2.1), which was used for the data analysis and for obtaining results presented in chapter 5, the Barrel Electromagnetic Calorimeter (BEMC, 4.2.2), the Vertex Position Detector (VPD, 4.2.3), the Muon Telescope Detector (MTD, 4.2.4), the Heavy Flavor Tracker (HFT, 4.2.5) or the Time-of-Flight detector which is used to determine the particles' velocity. The entire STAR experiment scheme can be seen in Fig. 4.2

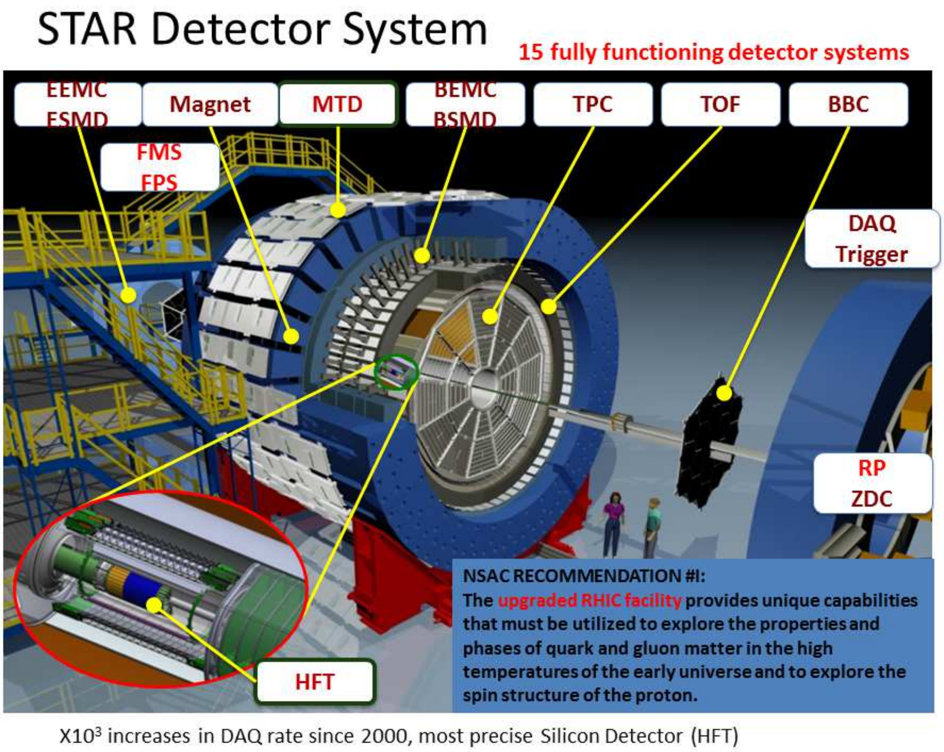

Figure 4.2: The STAR experiment scheme. Main parts, including magnet, TPC and BEMC are highlighted. Source: [47].

4.2.1 TPC

The Time Projection Chamber of the STAR detector is its most important part as it allows the detection of charged particles. The TPC is 4.2 m long, its diameter is 4 m and the entire volume is filled with gas (10 % methane, 90 % argon) in a uniform electric field E = 135 V.cm^{-}1, [11], defined by a conductive membrane at $z = 0$ (z-axis defined by the beam line). This allows precise z-coordinate measurement by measuring the drift time of the electrons produced after the ionization to the read-out caps at the ends of the TPC. The x and y coordinates are determined by hit signals in pads. One track can have up to 45 hits (the cut for this analysis was minimum 20 hits) as there are 45 layers of pads. The TPC has full azimuthal coverage and covers a pseudorapidity range of $\eta < |1.8|$ in the z-axis direction. It measures the particles' momentum and identifies the particles by measuring the energy loss ($\frac{\mathrm{d}E}{\mathrm{d}x}$) due to ionization as described by the Bethe-Bloch formula (or the Bichsel functions in STAR's case, fig. 4.3).

The TPC can measure the particle momentum in 100 MeV/c to 30 GeV/c range, [15]. The STAR TPC scheme can be seen in Fig. 4.4.

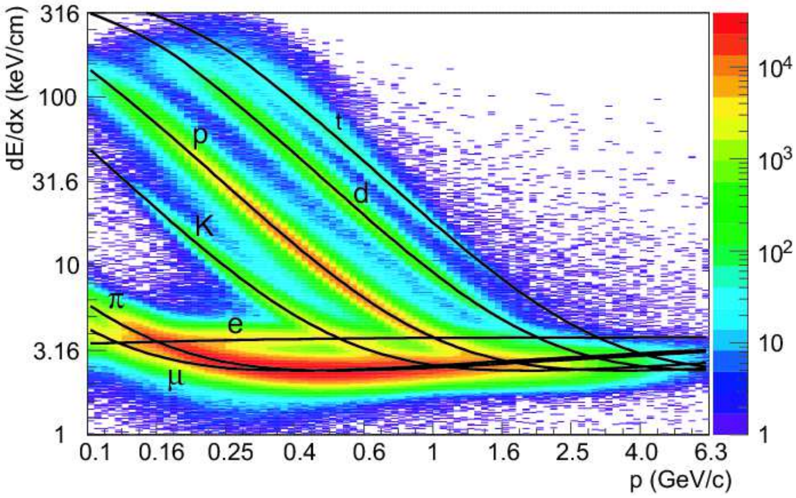

Figure 4.3: dE/dx versus momentum plot for common charged particles. The black lines are the Bichsel functions. Source: [48].

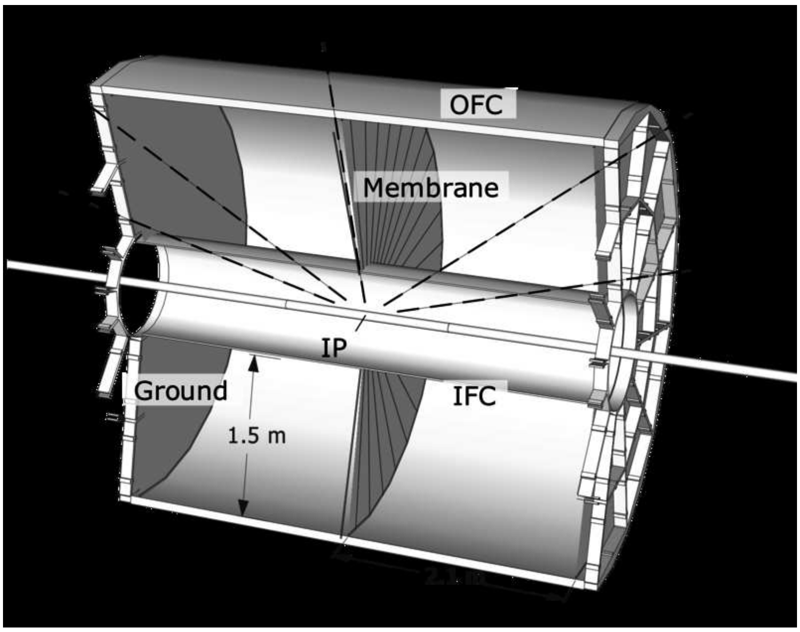

Figure 4.4: The STAR Time Projection Chamber. Main features are highlighted, IP - Intersection Point, IFC - Inner Field Cage, OFC - Outer Field Cage. Source: [47].

4.2.2 BEMC

The Barrel Electromagnetic Calorimeter is on the outside of the TPC, with inner radius of 2.2 m and outer radius o 2.5 m. It is composed of 4800 towers, each consisting of 20 layers of lead and 19 layers of plastic scintillator. The BEMC covers the full azimuthal angle and pseudorapidity range of $\eta < |1|$ and is able to trigger on every bunch crossing at the intersection point. Low-mass particles (electrons) will deposit its entire energy in the BEMC while the more massive hadrons will deposit only a fraction of it, making the electrons easier to identify. The BEMC scheme can be seen in Fig. 4.5.

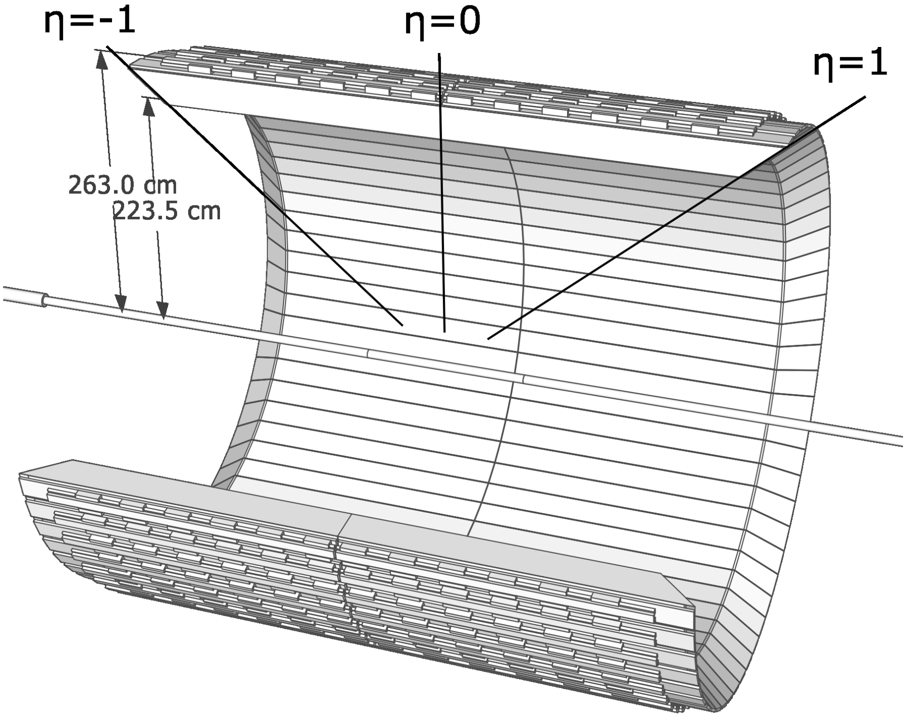

Figure 4.5: The Barrel Electromagnetic Calorimeter scheme. Source: [47].

4.2.3 VPD

The Vertex Position Detector is completely implemented in the STAR trigger system. Its main function is to measure the difference of trigger times from the two parts of the detector located 5.6 m from $z = 0$ along the beam line on both sides of the experiment. The time difference than allows precise reconstruction of the z-coordinate of the event. For further details on the VPD see [49].

4.2.4 MTD

The Muon Telescope Detector at the STAR experiment is a newly installed detector on the outside of the magnet, which is used to detect muons, allowing the usage of the dimuon channel to detect quarkonia. This should allow for better quarkonia related measurements, since the dimuon channel is very clean compared to the now-used dielectron channel. The muon identification efficiency is up to 90 %. One of the MTD modules can be seen in Fig. 4.6. For more details on the MTD see [51].

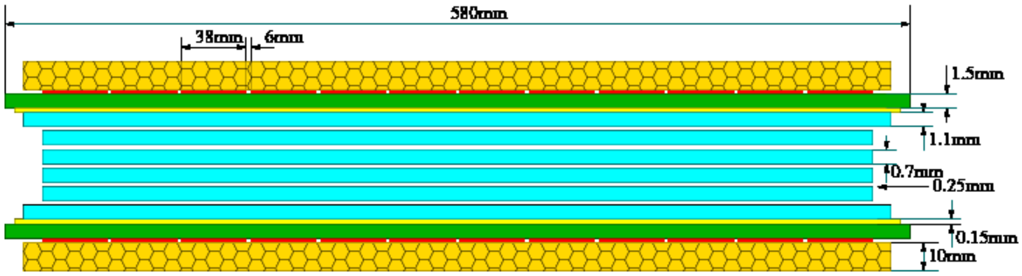

Figure 4.6: Side view of one of the MTD modules showing different layers - honey combs (yellow), strips (red), PCboards (green), mylards (light yellow) and glasses (light blue). Source: [50].

4.2.5 HFT

The Heavy Flavor Tracker was installed in 2014 and serves as a primary detector of heavy flavored particles (e.g. D and B mesons) at STAR. This detector allows for the direct detection of heavy flavored partilces' decay products which severly reduces the background in the measurements. The HFT consists of silicon detectors arranged in four concentric cylinders (two outer layers are composed of pads and strips, the inner two of monolithic pixel detectors) very close to the center of the STAR experiment. The HFT scheme is illustrated in Fig. 4.7, more on HFT can be seen in [53].

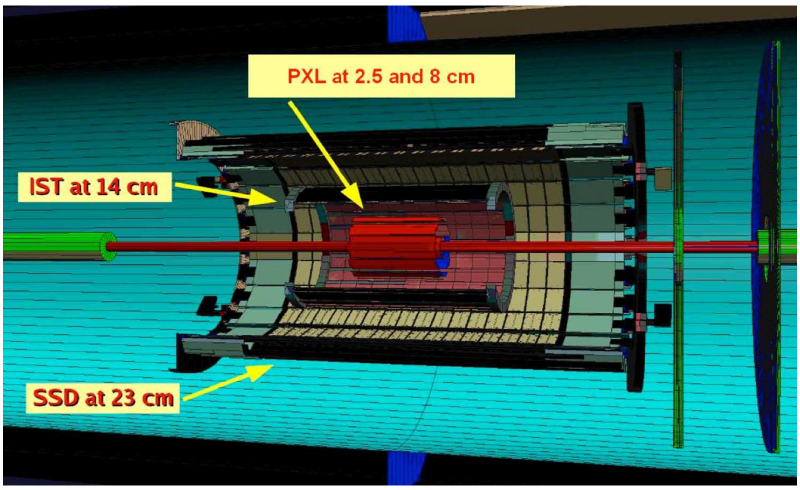

Figure 4.7: The Heavy Flavor Tracker at STAR scheme. The four detector layers are depicted. Source: [52].

Chapter 5

Results

In this chapter the results of Υ meson production are presented. The data used for the analysis were taken from the 2011 RHIC run at $\sqrt{s_{NN}} = 200$ GeV in Au-Au collisions. Used minimum bias data were in the PicoDst format. The Υ mesons were detected in the dielectron decay channel, the analysis cuts are described in sec. 5.1. The primary practical objective of this thesis was to obtain a dielectron invariant mass spectrum in the Υ mass range, where a distinct peak should be observable. However, this task has not been completed as of yet.

5.1 Analysis Cuts

Several cuts were applied to obtain tracks corresponding to dielectrons from the Υ meson decay. These cuts are summarized in the following table:

Analysis Cut	Value(s)
N_{fit}	$\geq$20
$\frac{N_{fit}}{N_{max}}$	0.51
DCA	1.5 cm
$Nsigma$	$\in <$-1,3$>$
$\lvert\eta\rvert$	$\leq$1
p_T	$\geq$ 4 GeV/c

Table 5.1: Table displaying the cuts used in the analysis. Cuts are further described in the text.

5.1.1 Track Selection

The requirements for a track to be accepted as a candidate for an electron (since positrons differ from electrons only in their charge, all cuts presented here apply for positrons as well and both are referred to as electrons) were as follows. The minimal number of fitted hits in the TPC was set to $N_{fit} \geq 20$ to assure sufficient precision of the track detection. The ratio of fitted hits versus the maximum possible hits in the TPC was $\frac{N_{fit}}{N_{max}} \geq 0.51$ to assure that one track is matched with only one particle. Finally, the Distance of Closest Approach between a reconstructed track and the primary vertex was set to DCA < 1.5 cm.

5.1.2 Electron Selection

Electrons were distinguished from other particles created in the collisions (mainly pions and protons) using their specific $\mathrm{d}E/\mathrm{d}x$ behavior. This results in a value called $Nsigma$ which is a measure of confidence level that a certain particle is in fact an electron (closer to $0 =$ more likely an electron). For this analysis, particles with $-1 \leq Nsigma \leq 3$ were taken as electrons. This range was selected because it is the optimal balance between keeping as many electrons as possible without contamination (mainly by pions). The distribution of particles in $Nsigma$ can be seen in Fig. 5.1, with cut described above shown as red lines.

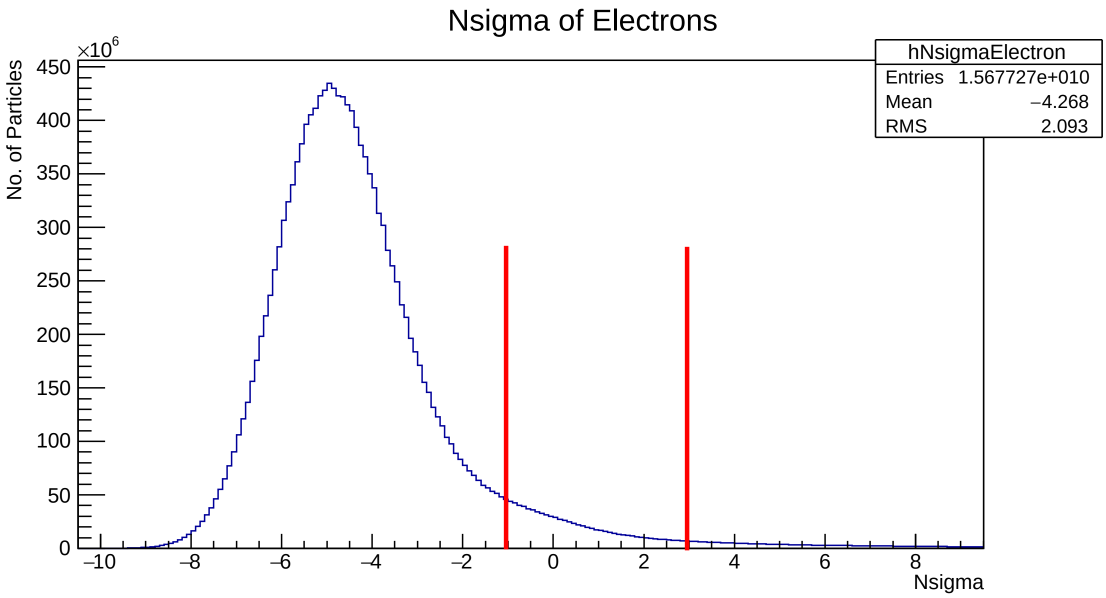

Figure 5.1: The distribution of charged particles in $Nsigma$, with red lines denoting applied cut on electrons.

5.1.3 Azimuthal Angle

Although there was no requirement of a cut on the azimuthal angle in which the particles move after the collision, their distributions in this angle ϕ are shown. In Fig. 5.2 the distribution of all charged particles can be seen. The most notable feature of this graph is the large drop-off approximately at $-1 \leq \phi \leq 0$. This was probably caused by a malfunction of a specific sector of the TPC and has no physical meaning. This did not affect the electron selection significantly as this effect is not observed in high-p_T electrons (5.3) which means that it only affected the detection of low-p_T particles. Aside from this section, the distribution appears symmetric.

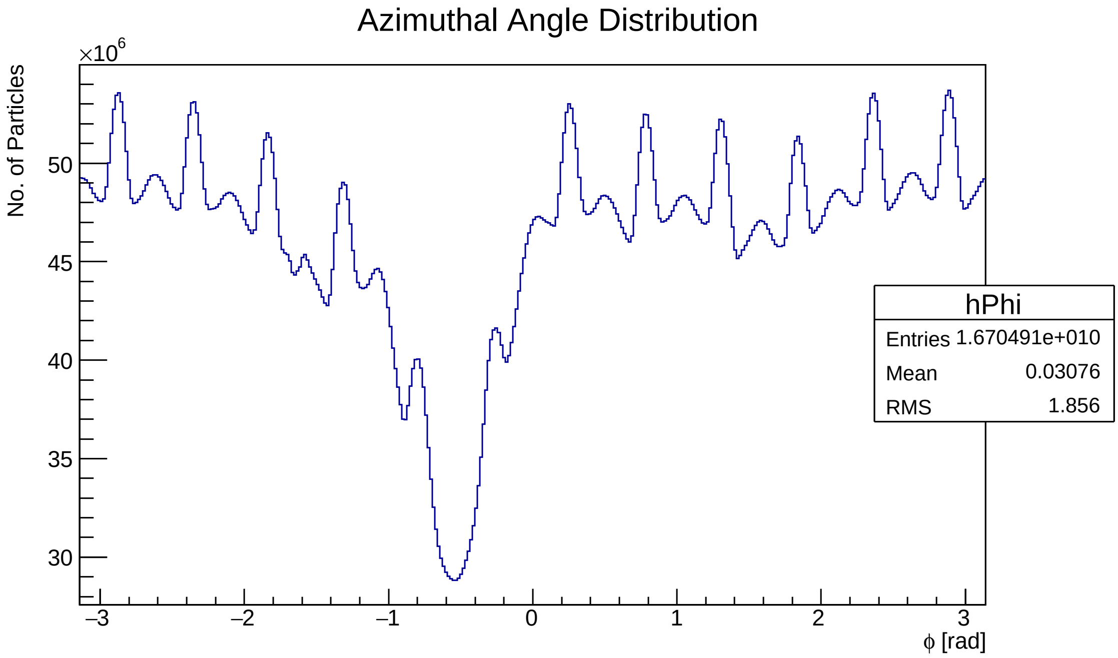

Figure 5.2: The azimuthal angle distribution of all charged particles. The nature of the irregularity between approx. -1 $\leq \phi \leq$ 0 is explained in the text.

In Fig. 5.3 the azimuthal angle distribution of electrons that meet all requirements (Tab. 5.1) can be seen. Somewhat surprising is the fact, that the irregularity shown in Fig. 5.2 is not present in this graph. The characteristic peaks in the spectrum are more prominent and sharp for selected electrons than for all charged particles. The distribution is symmetric as expected.

5.1.4 Pseudorapidity

Pseudorapidity can be described as a dimensionless measure of an angle at which the particles leave the primary vertex with respect to the z axis. The charged particle distribution can be seen in Fig. 5.4. The distribution appears symmetric, as was expected.

Because the future plan for this analysis was to include data taken by the calorimeter which covers the pseudorapidity range of $|\eta| \leq 1$, this cut was applied on the electrons. Another fact justifying the cut is the shape of the spectrum, which falls off rapidly at η close to $\pm$ 1 so very small portion of particles has higher $|\eta|$. However the shape of the spectrum of electrons after cuts looks very different with highest numbers of particles leave the primary vertex at a higher angle. The distribution after this and other cuts is shown in Fig. 5.5 and a slight asymmetry can be seen.

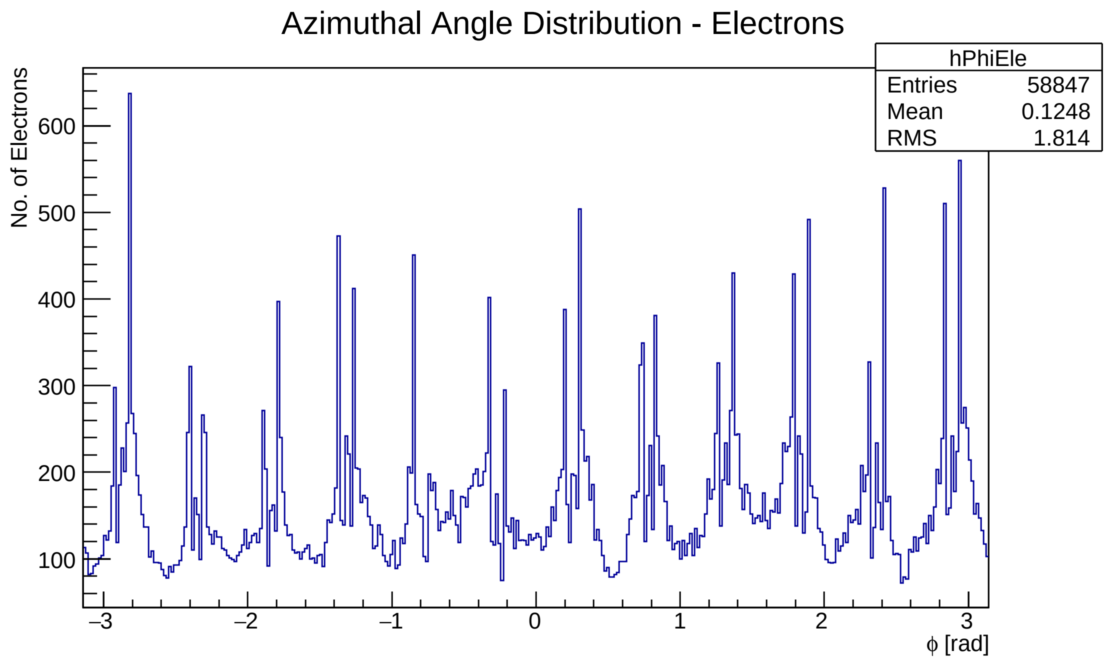

Figure 5.3: The azimuthal angle distribution of electrons (after applied cuts) showing periodical behavior.

5.1.5 Transverse Momentum

Transverse momentum is the momentum of a particle projected on a plane perpendicular to the beam axis, given by an equation

$$p_T = \sqrt{p_x^2 + p_y^2}. \tag{5.1}$$

The p_T distribution of all charged particles is shown in Fig. 5.6. The spectrum is falling very rapidly (faster than exponentially) as expected. There seems to be a maximum value at about 0.5 GeV/c.

Because the mass of the Υ meson is very large, the decay products such as dielectrons have typically very high transverse momenta. Therefore a cut $p_T > 4$ GeV/c was applied to distinguish these dielectrons. The distribution of electrons in p_T can be seen in Fig. 5.7, with a clearly shown cut-off.

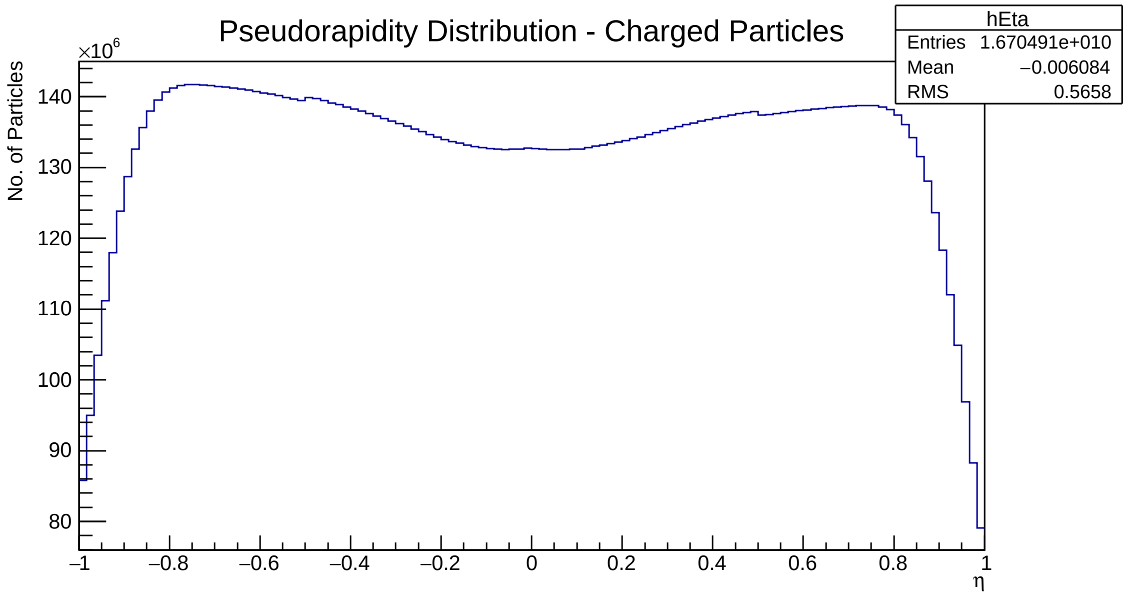

Figure 5.4: All charged particles' distribution in pseudorapidity which has an expected shape.

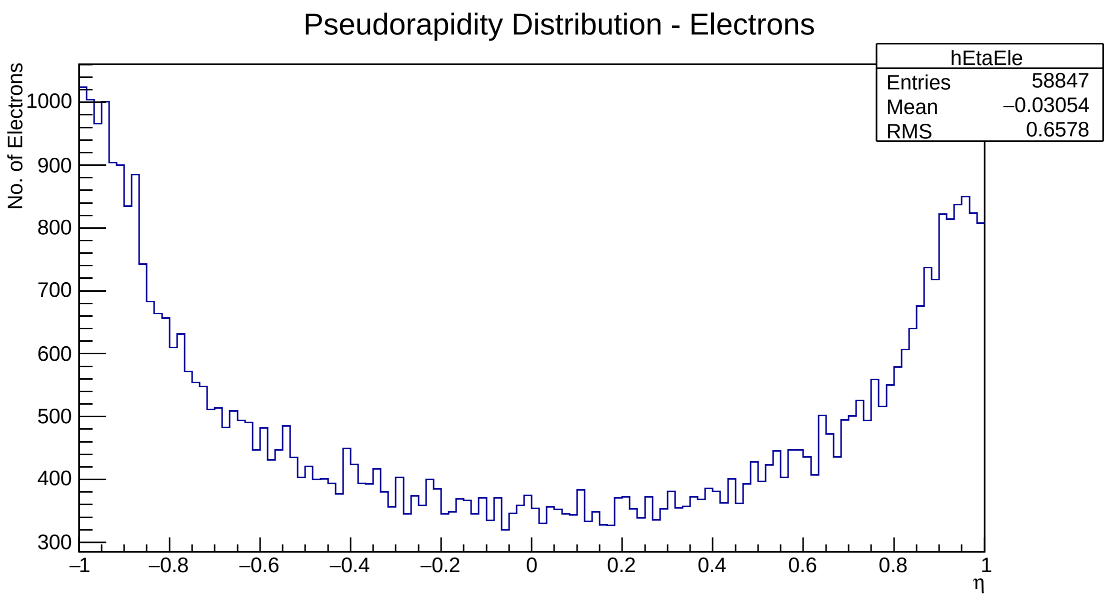

Figure 5.5: Selected electrons' distribution in pseudorapidity. The shape of this spectrum is very different from the spectrum of all charged particles - most high-p_T electrons leave the initial area at a higher polar angle.

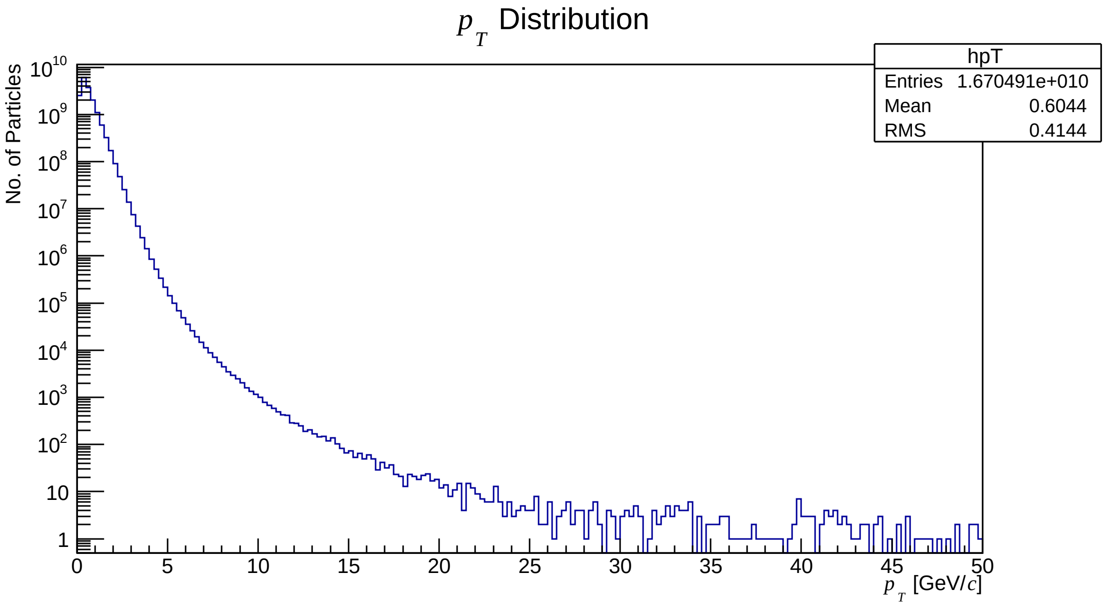

Figure 5.6: The p_T dependence of the number of all charged particles. The spectrum is very rapidly falling.

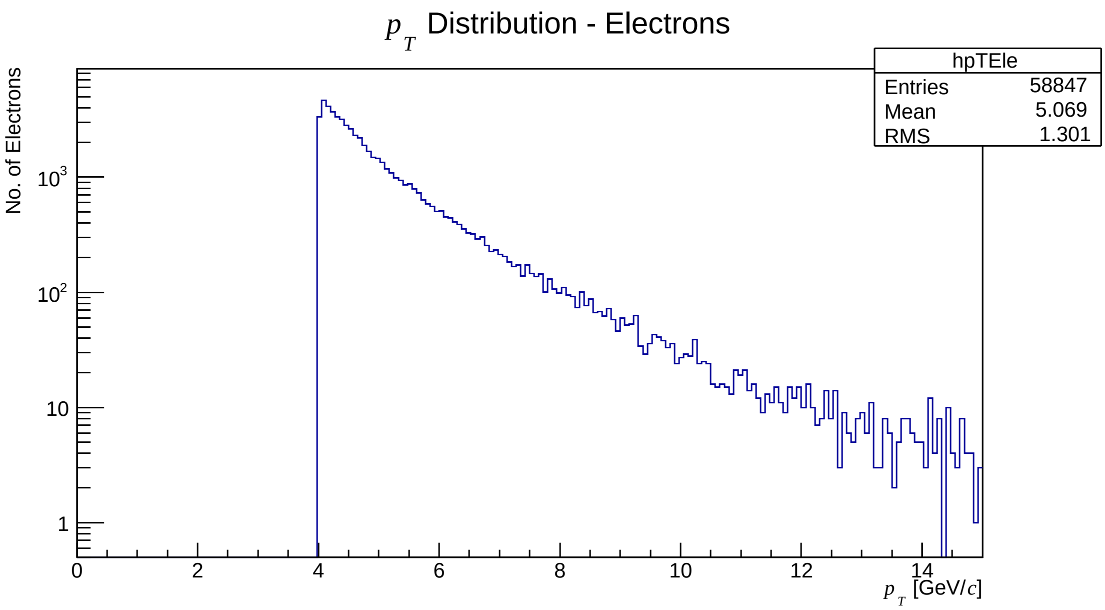

Figure 5.7: The distribution of selected electrons in p_T. Because of the large mass of the Υ meson, the dielectrons originating from its decay are moving with high p_T and so the spectrum can be cut off at $p_T = 4$ GeV/c.

Conclusion

Quark-gluon plasma is a state of matter assumed to exist in the early Universe. It is recreated today in heavy-ion collisions at high energies at circular colliders such as LHC or RHIC. As it is impossible to study the QGP directly, several probes, namely elliptic flow, jet quenching and quarkonia production suppression, are used to determine the physical properties of the QGP. The Υ meson serves as an excellent probe since it provides us with three detectable states with very different binding energies. At RHIC and LHC energies, only the $\Upsilon(2S)$ and $\Upsilon(3S)$ states are suppressed while there is no direct $\Upsilon(1S)$ suppression. The main goal of this thesis was to reconstruct the invariant mass spectrum of the Υ meson in the dielectron channel. Used data were the 2011 STAR data from Au-Au $\sqrt{s_{NN}} = 200$ GeV collisions. Dielectrons were detected using the STAR TPC and several analysis cuts based on technical (such as the pseudorapidity coverage) and physical properties (such as the transverse momentum cut-off) were applied to select dielectrons coming from Υ meson decays. The invariant mass spectrum which should have an observable peak in the Υ meson mass range has not been successfully reconstructed as of yet, but the process is not finished. Meanwhile, other minor tasks, such as the azimuthal angle distribution, pseudorapidity distribution and transverse momentum spectra for all charged particles and for electrons, were completed successfully. Overall, the ultimate goal which was to learn about the physics of the Υ meson and to understand the data structure at STAR was accomplished. This analysis also served as a learning experience and training for the Υ meson analysis methodology and work with the STAR analysis software. This gained experience will be greatly used in the future work, which should include the analysis of the Υ production in the 2015 p-Au STAR data.

References

[1] J. Glick, Rochester Institute of Technology, personal site, 1/13/2012, [online, cit. 2/24/16], https://people.rit.edu/~jng4080/Images/Information/Periodic%20Tables/

[2] C. O'Luanaigh, "New results indicate that new particle is a Higgs boson", CERN, 1/27/2015, [online, cit. 2/24/16], http://home.cern/about/updates/2013/03/new-results-indicate-new-particle-higgs-boson

[3] "Neutrino Oscillations", NP in Physics, Class for Physics of the Royal Swedish Academy of Sciences, 10/6/2015

[4] "The Nobel Prize in Physics 2015", Nobel Media AB, 2/19/2016, [online, cit. 2/24/16], http://www.nobelprize.org/nobel_prizes/physics/laureates/2015/

[5] A. Toia, "Participants and spectators at the heavy-ion fireball", University of Padua/INFN, CERN Courier, 4/26/2013, [online, cit. 2/25/16], http://cerncourier.com/cws/article/cern/53089

[6] "More Details on the ALICE V0 Detector", CERN, 7/24/2014, [online, cit. 3/11/16], http://alipub-dev.web.cern.ch/detectors/more-details-alice-v0-detector

[7] M. Miller *et al.*, "Glauber Modeling in High Energy Nuclear Collisions", 1/17/2007, arXiv:nucl-ex/0701025

[8] Á. Mócsy, P. Sorensen, A. Doig, "The Sound of the Little Bang", [online, cit. 2/25/16], http://soundofthelittlebang.com/atomsmashing.html

[9] T.K. Nayak, "Heavy Ions: Results from the Large Hadron Collider", 1/2015, arXiv:1201.4264 [nucl-ex]

[10] M. Gyulassy, "The QGP Discovered at RHIC", 3/12/2004, arXiv:nucl-th/0403032v1

[11] O. Hajkova, "Quarkonia production in heavy-ion collision at RHIC and LHC", Bachelor Thesis, FNSPE CTU in Prague, 2009

[12] T. Dorigo "New CMS Results", 10/27/2014, [online, cit. 3/8/16], http://www.science20.com/a_quantum_diaries_survivor/new_cms_results-147752

[13] Z. Fodor, S.D. Katz, "The Phase Diagram of Quantum Chromodynamics", 8/23/2009, arXiv:0908.3341v1 [hep-ph]

[14] U. Heinz, M. Jacob, "Evidence for a New State of Matter: An Assessment of the Results from the CERN Lead Beam Programme", 2/16/2000, arXiv:nucl-th/0002042v1

[15] R.J. Reed, "Υ production at $\sqrt{s_{NN}} = 200$ GeV in p+p and Au+Au collisions at STAR", Dissertation Thesis, UC Davis, 2011

[16] A. Mocsy, "Potential Models for Quarkonia", 11/3/2008, arXiv:0811.0337 [hep-ph]

[17] T. Matsui, H. Satz, "J/ψ Suppression by Quark-gluon Plasma Formation", Phys. Let. B, vol. 178, no. 4, 10/9/1986

[18] P. Sorensen, "Soft Probes Program at RHIC ", NSAC Subcommittee 2012, BNL

[19] E.L. Bratkovskaya, O. Linnyk, W. Cassing, "Electromagnetic Probes of the QGP", 9/15/2014, arXiv:1409.4190 [nucl-th]

[20] A. Saini, S. Bhardwaj, "Elliptic Flow in Heavy Ion Collisions", 2014, JNPP, DOI: 10.5923/j.jnpp.20140406.02

[21] S.A. Voloshin *et al.* "Collective phenomena in non-central nuclear collisions", 10/30/2008, arXiv:0809.2949v2 [nucl-ex]

[22] B.I. Abelev *et al.*, "Mass, Quark-number, and $\sqrt{s_{NN}}$ Dependence of the Second and Fourth Flow Harmonics in Ultra-relativistic Nucleus-nucleus Collisions", 1/6/2007, arXiv:nucl-ex/0701010

[23] V. Wagner, "Srážky atomových jader olova produkují kvark-gluonové plazma" [czech text], UJF CAS, 12/2/2010, [online, cit. 3/11/16], `http://hp.ujf.cas.cz/~wagner/popclan/lhc/vytrysky_LHC.htm`

[24] D. d'Enterria, "Jet Quenching", CERN, 4/19/2009, arXiv:0902.2011v2 [nucl-ex]

[25] F. Arleo *et al.*, "Quarkonium Suppression in Heavy-ion Collisions from Coherent Energy Loss in Cold Nuclear Matter", JHEP 1410 (2014), arXiv:1407.5054 [hep-ph]

[26] "Probing QCD Phase Diagram using Conserved Charge Fluctuations", Lattice Gauge Theory Group, Nuclear Theory, Brookhaven National Laboratory, [online, cit. 6/1/16], `http://quark.phy.bnl.gov/~swagato/USQCD/`

[27] R.A. Lacey *et al.*, "Has the QCD Critical Point Been Signaled by Observations at RHIC?", 2/14/2007, arXiv:nucl-ex/0609025v5

[28] R.A. Lacey, "Indications for a critical end point in the phase diagram for hot and dense nuclear matter ", Quark Matter 2015, Kobe, 9/28/2015

[29] L. Kumar, "STAR Results from the RHIC Beam Energy Scan-I", STAR collaboration, 11/6/2012, arXiv:1211.1350v1 [nucl-ex]

[30] A. Andronic *et al.*, "Heavy-flavour and Quarkonium Production in the LHC Era: From Proton-proton to Heavy-ion Collisions", 6/12/2015, arXiv:1506.03981v1 [nucl-ex]

[31] W. De Boer, "The Discovery of the Higgs Boson with the CMS Detector and its Implications for Supersymmetry and Cosmology ", CMS collaboration, 9/3/2013, arXiv:1309.0721v1 [hep-ph]

[32] J. Fodorova, "Heavy quarkonia production at the STAR experiment", Bachelor Thesis, FNSPE CTU in Prague, 2014

[33] C. Amsler *et al.*, Particle Data Group, PL B667, 1 (2008) and 2009 partial update for the 2010 edition, [online, cit. 3/15/16] `http://pdg.lbl.gov`

[34] E. Beveren, G. Rupp, "Mass and width of the $\Upsilon(4S)$)", 10/6/2009, arXiv:0910.0967v1 [hep-ph]

[35] "Observation of a New χ_b State in Radiative Transitions to $\Upsilon(1S)$ and $\Upsilon(2S)$ at ATLAS", the ATLAS collaboration, 4/11/2012, arXiv:1112.5154v5 [hep-ex]

[36] "First Measurement of η_b (ground state of b/anti-b quark pair)" BaBar collaboration, University of Maryland, 2008, [online, cit. 3/15/16], `http://www.physics.umd.edu/news/News_Releases/BaBar2008.htm`

[37] S.W. Herb *et al.*, "Observation of a Dimuon Resonance at 9.5 GeV in 400 GeV Proton-nucleus Collisions", 7/1977, FERMILAB-Pub-77/58-EXP 7100.288

[38] A. Adare *et al.*, $\Upsilon(1S + 2S + 3S)$ production in d+Au and p+p collisions at $\sqrt{s_{NN}}$ =200 GeV and cold-nuclear-matter effects, 11/16/2012, arXiv:1211.4017v1 [nucl-ex]

[39] A.R. Kesich, "Upsilon Production and Suppression as Measured by STAR in p + p, d + Au, and Au + Au Collisions at $\sqrt{s_{NN}} = 200$ GeV", Dissertation Thesis, UC Davis, 2014

[40] L. Adamczyk *et al.*, "Υ production in U+U collisions at $\sqrt{s_{NN}} = 193$ GeV with the STAR experiment", STAR collaboration, 3/23/2016, ?arXiv?

[41] B. Abelev *et al.*, "Suppression of $\Upsilon(1S)$ at forward rapidity in Pb–Pb collisions at $\sqrt{s_{NN}} = 2.76$ TeV", 10/30/2014, arXiv:1405.4493v3 [nucl-ex]

[42] "Measurement of $\Upsilon(nS)$ production with p+Pb collisions at $\sqrt{s_{NN}} = 5.02$ TeV and pp collisions at $\sqrt{s_{NN}} = 2.76$ TeV", ATLAS collaboration, Quark Matter 2015, Kobe, 9/26/2015

[43] A. Abdulsalam, "Bottomonium production in p+p, p+Pb and Pb+Pb collisions with CMS", CMS collaboration, Quark Matter 2014, Darmstadt, 5/21/2015

[44] M. Jo, "CMS bottomonia results from Run I", CMS collaboration, Quark Matter 2015, Kobe, 9/30/2015

[45] A. Accardi *et al.*, "Electron Ion Collider: The Next QCD Frontier", 11/30/2014, arXiv:1212.1701v3 [nucl-ex]

[46] K. Walsh, "Accelerating Particles Accelerates Science — With Big Benefits for Society", 3/13/2013, [online cit. 4/16/16], `https://www.bnl.gov/rhic/news2/news.asp?a=3758&t=today`

[47] "The STAR Experiment", [online, cit. 4/19/16], `https://drupal.star.bnl.gov/STAR`

[48] B.I. Abelev *et al.*, "Hadronic resonance production in d+Au collisions at $\sqrt{s_{NN}}$ = 200 GeV at RHIC", 8/22/2008, arXiv:0801.0450v2 [nucl-ex] "

[49] W.J. Llope *et al.*, "The STAR Vertex Position Detector", 3/26/2014, arXiv:1403.6855 [physics.ins-det]

[50] C. Yang *et al.*, "Calibration and performance of the STAR Muon Telescope Detector using cosmic rays", 2/5/2014, arXiv:1402.1078v1 [physics.ins-det]

[51] T.C. Huang *et al.*, "Muon Identification with Muon Telescope Detector at the STAR Experiment", 1/2/2016, arXiv:1601.02910v1 [physics.ins-det]

[52] L. Yarris, "Heavy Flavor Tracker for STAR", 2/18/2014, [online, cit. 5/10/16], `http://newscenter.lbl.gov/2014/02/18/heavy-flavor-tracker-for-star/`

[53] J. Schambach *et al.*, "The STAR Heavy Flavor Tracker (HFT)", 9/2014,10.3204/DESY-PROC-2014-04/83, C14-08-24, p.659-664